



Laboratory study of the breaking and energy distribution of internal solitary waves over a ridge

Yulin Guo¹, Xu Chen^{1,†}, Qun Li² and Jing Meng¹

¹Key Laboratory of Physical Oceanography, Ocean University of China and Qingdao National Laboratory for Marine Science and Technology, Qingdao 266100, PR China

²MNR Key Laboratory for Polar Science, Polar Research Institute of China, Shanghai 200136, PR China

(Received 26 November 2023; revised 13 May 2024; accepted 11 July 2024)

The breaking and energy distribution of mode-1 depression internal solitary wave interactions with Gaussian ridges are examined through laboratory experiments. A series of processes, such as shoaling, breaking, transmission and reflection, are captured completely by measuring the velocity field in a large region. It is found that the maximum interface descent (a_{max}) during wave shoaling is an important parameter for diagnosing the type of wave–ridge interaction and energy distribution. The wave breaking on the ridge depends on the modified blockage parameter ζ_m , the ratio of the sum of the upper layer depth and a_{max} to the water depth at the top of the ridge. As ζ_m increases, the interaction type transitions from no breaking to plunging and mixed plunging–collapsing breaking. Within the scope of this experiment, the energy distribution can be characterized solely by ζ_m . The transmission energy decreases monotonically with increasing ζ_m , and there is a linear relationship between ζ_m^2 and the reflection coefficient. The value of a_{max} can be determined from the basic initial parameters of the experiment. Based on the incident wave parameters, the depth of the upper and lower layers, and the topographic parameters, two new simple methods for predicting a_{max} on the ridge are proposed.

Key words: internal waves, stratified flows, topographic effects

1. Introduction

Internal solitary waves (ISWs) are typical nonlinear waves that occur in the stratified ocean, with a maximum amplitude located in the oceanic interior; these waves can propagate over long distances after generation while maintaining their basic wave characteristics (Grimshaw *et al.* 1998, 2010; Helfrich & Melville 2006; Alford *et al.* 2010; Ramp *et al.* 2019). They are characterized by large amplitudes, strong velocities, strong

† Email address for correspondence: chenxu001@ouc.edu.cn

shear and short periods, which can draw the thermocline downwards or upwards for tens to hundreds of metres, resulting in surface velocities of $1\text{--}2\text{ m s}^{-1}$ (Pinkel 2000; Alford *et al.* 2010; Farmer *et al.* 2011; Huang *et al.* 2016). Due to these characteristics, ISWs have an important impact on the safety of underwater vehicles and marine structures (Song *et al.* 2011; Wang *et al.* 2018, 2022). As ISWs shoal and break over the seabed topography, they release considerable amounts of energy that can promote local turbulent mixing and the resuspension of sediments and nutrients in the ocean (Sandstrom & Elliott 1984; Reeder, Ma & Yang 2011; Boegman & Stastna 2019). ISWs are also an effective pathway for transferring energy from large-scale barotropic tides to small-scale turbulence, and cumulatively this energy is an integral part of the oceanic energy budget (Bourgault & Kelley 2003; Zhang *et al.* 2023).

The ISWs generated by barotropic tides over varying seabed topographies are common in marginal seas worldwide (Jackson 2007). The onshore propagation of ISWs interacts with the seabed topography and eventually dissipates on the continental shelf slope (Lamb 2014; Davis *et al.* 2020; Jones *et al.* 2020). In the process of wave shoaling, fission, polarity conversion and other evolutionary processes will occur (Orr & Mignerey 2003; Ramp *et al.* 2022; Sinnott *et al.* 2022), as well as the breaking and mixing process caused by shear instability, convection instability and benthic boundary layer instability (Moum *et al.* 2003; Barad & Fringer 2010; Lien *et al.* 2014; Boegman & Stastna 2019; Xu & Stastna 2020; Chang *et al.* 2021). All these processes promote the dissipation of ISWs and transform their energy into microscale turbulence.

Due to the importance of ISW shoaling and breaking, how to characterize the breaking of ISWs in terms of predetermined factors has become a hot topic. Several studies have analysed the shoaling, breaking and energy distribution of ISWs on uniform slopes (Helfrich 1992; Michallet & Ivey 1999; Boegman, Ivey & Imberger 2005; Bourgault & Kelley 2007; Lamb & Nguyen 2009; Aghsaee, Boegman & Lamb 2010; Sutherland, Barrett & Ivey 2013; Carr *et al.* 2019; Nakayama *et al.* 2019; Hartharn-Evans *et al.* 2021). Through laboratory experiments, Boegman *et al.* (2005) found that the breaking mechanism of internal waves depends on the ratio of the topographic slope to the incident wave slope. Referring to the breaking type of surface waves, they classified internal wave breaking into spilling, plunging and collapsing, and introduced the internal Iribarren number (Ir) to delineate different breaking types:

$$Ir = \frac{s}{\sqrt{s_w}}, \quad (1.1)$$

where s is the topographic slope, $s_w = a/L_w$ is the wave slope, a is the incident wave amplitude, and L_w is the wavelength. Sutherland *et al.* (2013) adjusted and expanded the classification scheme of ISW breaking, which can be separated into no breaking, surging breaking, collapsing breaking, plunging breaking and plunging–collapsing breaking. By analysing previous experimental and numerical results, Nakayama *et al.* (2019) defined a dimensionless parameter based on weakly nonlinear theory (KdV theory) $B_{ISW} = (s/s_w) Re_{ISW}^2$, which depends on the wave slope, topographic slope and wave Reynolds number ($Re_{ISW} \equiv \alpha ah_0/\nu$, where α is the coefficient of the nonlinear term in the KdV equation, h_0 is the harmonic mean of the water depth, and ν is the kinematic viscosity). Plunging breaking occurs when $B_{ISW} > 7 \times 10^6$, while collapsing breaking occurs when $B_{ISW} < 7 \times 10^6$. Hartharn-Evans *et al.* (2021) combined numerical simulations and experiments to explore the influence of stratification on the shoaling and breaking of ISWs, and found that surface stratification (density gradient throughout the upper layer) can inhibit plunging, while a broad tanh profile can simultaneously inhibit collapsing and plunging.

Breaking and energy distribution of ISWs over a ridge

When an ISW breaks on a slope, part of the energy dissipates locally, and part is reflected. Regarding the reflection coefficient on uniform slopes, the experimental results of Helfrich (1992) and Michallet & Ivey (1999) showed that the ratio of reflected energy generated by ISWs impinging on the slope to total energy depends on the wavelength and topographic scale ratio. The numerical simulation of Bourgault & Kelley (2007) showed that Michallet & Ivey (1999) underestimated the reflection coefficient due to ignoring the friction effect, and proposed a parametrization scheme dependent on Ir , namely $R = 1 - e^{-Ir/Ir_0}$, where $Ir_0 = 0.78 \pm 0.02$ (95 % confidence intervals). Lamb & Nguyen (2009) combined the available potential energy flux with the kinetic energy flux to calculate the reflection coefficient, and found that compared to the approximate calculation method of Bourgault & Kelley (2007), the correct estimation of available potential energy flux could reduce the predicted reflection coefficient by a maximum of 0.1. Aghsaei *et al.* (2010) believed that the calculation of the reflection coefficient at the toe of the slope would ignore the energy dissipation caused by viscosity before incident wave breaking and after reflection wave generation. The reflection coefficient based on the breaking point has been introduced, and the coefficient Ir_0 of the parametrized scheme of Bourgault & Kelley (2007) was revised to 0.65.

The breaking location of ISWs on slopes can be predicted by the initial stratification conditions and the incident wave parameters (Helfrich 1992; Vlasenko & Hutter 2002; Aghsaei *et al.* 2010; Sutherland *et al.* 2013; Cavaliere *et al.* 2021). The experimental results of Helfrich (1992) showed that breaking occurs when the non-dimensional wave amplitude ($a/(h_b - h_m)$, where h_b is the water depth at the breaking point, and h_m is the depth of the undisturbed interface) exceeds 0.4. Vlasenko & Hutter (2002) proposed an ISW breaking criterion that is dependent on the topographic slope (represented by slope angle $\gamma = \arctan(s)$), which was based on the selection of stratification conditions, topography and wave parameters of the Andaman Sea and Sulu Sea:

$$\frac{a}{h_b - h_m} \geq \frac{0.8^\circ}{\gamma} + 0.4. \quad (1.2)$$

For the prediction of the maximum interfacial descent (a_{max}) at the breaking depth, Sutherland *et al.* (2013) approximated the waveforms of internal waves before breaking into a right triangle shape (especially for plunging–collapsing breaking). Assuming that the area of the right triangle (the volume per unit width of the upper layer fluid below the initial depth of the interface) is equal to the approximate area of the incident wave ($S_{ISW} = aL_w$), a prediction formula for a_{max} has been established:

$$a_{max} = \sqrt{4saL_{sw}}, \quad (1.3)$$

where L_{sw} is half of the width at half-amplitude. Based on the analysis method of Sutherland *et al.* (2013), Cavaliere *et al.* (2021) modified the area of the initial wave by using extended KdV and Miyata–Choi–Camassa theories to obtain the prediction formula of the breaking location and depth.

For the evolution of ISWs over submerged obstacles (Wessels & Hutter 1996; Sveen *et al.* 2002; Chen 2007, 2009; Sutherland, Keating & Shrivastava 2015), the blockage parameter (ζ) was identified as another important parameter:

$$\zeta = \frac{a + h_1}{h_1 + h_2 - H_r}, \quad (1.4)$$

where h_1 and h_2 represent the upper and lower water depths, respectively, and H_r represents the height of the ridge. The laboratory experiment of Sveen *et al.* (2002) studied

the interaction of ISWs with triangular ridges, classifying the degree of interaction (as weak, moderate or strong) according to the blockage parameter and the dimensionless velocity over the ridge crest. Strong interaction occurs when $\zeta > 0.6$, and the breaking of ISWs results in intense turbulent mixing. Chen (2009) also described the degree of interaction in terms of wave energy based on the blockage parameter, and developed a statistical method to classify the types of interaction (Chen 2010). For mode-2 ISWs under symmetric stratification ($h_1 = h_2$), a similar blockage parameter ($a/(h_2 - h_t - H_r)$, where h_t is the pycnocline half-width) is used to classify the wave–ridge interaction strength, with a parameter exceeding 0.5 indicating wave breaking conditions (Deepwell *et al.* 2017, 2019). For the evolution and breaking of ISWs over a ridge, Hsieh *et al.* (2015) and Zhu *et al.* (2016) analysed the variation in wave parameters and energy through numerical simulations, and Lin *et al.* (2021) analysed the breaking structure and dissipation through laboratory experiments. In the other case, as the ISW passes over a small-amplitude, broad ridge, instability occurs near the crest of the topography in the form of a roll-up of vorticity, whereas the dissipation of wave energy is minimal (Harnanan, Soontiens & Stastna 2015; Harnanan, Stastna & Soontiens 2017).

The energy distribution of ISWs on the ridge exhibits both reflective and transmissive characteristics, which distinguishes it from the slope intersecting the pycnocline in the two-dimensional (2-D) case. Chen (2009) used the blockage parameter to characterize the transmitted and reflected energy. Zhu *et al.* (2016) described the varying trends of energy dissipation, transmission and reflection coefficients through the empirical formula of multiplying the blockage parameter and nonlinear parameter. Sutherland *et al.* (2015) non-dimensionalized the incident amplitude through the critical amplitude (dependent on topography and initial stratification), and provided a parametrized scheme for calculating the reflection and transmission coefficients.

The breaking and energy distribution of ISWs over a ridge have been investigated in previous studies based on laboratory experiments and numerical simulations. However, when selecting the interaction degree factor, the influence of the ridge height was mainly considered without considering the ridge slope simultaneously. At the field scale, the fractal structure of the seafloor gives rise to the presence of multiscale superposition of the topography. For example, gentler shelf slope areas have average slope about 0.03 to 0.07 (Cacchione, Pratson & Ogston 2002), which is much larger than the wavelength scale of ISWs. In the case of steeper slopes, the characteristic width of the bumpy topography, underwater banks and seamounts are comparable to the wavelengths of typical large-amplitude ISWs (Smith 1988; Wessel 2001; Vlasenko 2005; Xie *et al.* 2019). The variable horizontal and vertical scales of the seafloor result in a broad range of dimensionless parameters that control the type of interaction between the ISW and topography (table 1). Consequently, it is imperative to examine the combined effects of variations in topographic height and slope. This paper focuses on the case where the horizontal scale of the topography is comparable to the ISW wavelength, and the topographic height is comparable to the total water depth, a condition under which the topography has the most noticeable effect on the ISW (Sveen *et al.* 2002; Sutherland *et al.* 2015).

Regarding laboratory experiments, the research still lacks a complete description of the wave–ridge interaction. In this paper, a series of processes, such as shoaling, breaking, transmission and reflection of the interaction between the ISW and the Gaussian topography, are captured completely by measuring the velocity field in a large region. The laboratory experiments were used to systematically analyse the breaking types and dynamic processes of the wave–ridge interaction to study the energy distribution, the

Dimensionless parameter	Range		
	This experiment	Laboratory scale	Field scale
Amplitude (a/h_1)	0.48–2.36	0.2–2.1	0.1–3.0
Blockage parameter (ζ)	0.32–1.23	0.1–1.4	0.33–1.75
Iribarren number (I_r)	0.50–2.20	0.2–2.8	$O(10^{-3})$ –2.8
Wavelength/topographic length (L_w/L_s)	0.50–1.73	0.08– ∞	$O(10^{-2})$ – $O(10^0)$

Table 1. The dimensionless parameter ranges in this experiment and a comparison between the predominant ranges of dimensionless parameters in laboratory scale and field scale. The parameter ranges in laboratory scale and field scale refer to figures and tables from previous studies (Michallet & Ivey 1999; Sveen *et al.* 2002; Boegman *et al.* 2005; Vlasenko 2005; Chen 2009; Aghsaei *et al.* 2010; Alford *et al.* 2010; Bourgault, Janes & Galbraith 2011; Sutherland *et al.* 2013, 2015; Xie, He & Cai 2019; Davis *et al.* 2020; Ghassemi, Zahedi & Boegman 2021; Hartharn-Evans *et al.* 2021).

spatiotemporal structure of the turbulence, and the details of the breaking process. A dimensionless parameter that accounts for both ridge height and slope is introduced to characterize the degree of interaction. The study of the distribution trends of the breaking type, breaking position and breaking depth is helpful in analysing the mixing process, sediment resuspension process, and transport of material caused by internal waves. It can also be used to assist in the exploration of the energy distribution, which is useful for analysing the effect of internal waves on the oceanic energy budget.

The paper is structured as follows. The experimental set-up, definition and calculation of the basic parameters are introduced in § 2. In § 3, the basic characteristics and evolution of the ISW over the ridge are evaluated, and the breaking type and breaking time scale are analysed. In § 4, a method for predicting the maximum interface descent that can reflect the shoaling effect of internal waves is given. In addition, a prediction scheme for the type of breaking and energy distribution based on the maximum interface descent is also given. Finally, the results are summarized in § 5.

2. Experimental methods

2.1. Experimental set-up

Mode-1 depression ISWs were generated in an approximately two-layer stratified fluid using the standard lock-release method (Kao, Pan & Renouard 1985). The flume was 6 m long, 0.5 m high and 0.24 m wide (figure 1). The left-hand side of the flume was a wave-generating region. Before entering the observation region, the fluid that was released by the lock-release method had evolution distance up to 2 m, which made it adaptable to the characteristics inherent to an ISW. The centre of the flume was an experimental observation region with a 2-D Gaussian ridge, and the right-hand side was placed with a uniform slope for wave absorption.

The Gaussian ridge has constant height $H_r = 16$ cm and a variable standard deviation of the Gaussian function (σ) to account for changes in the topographic length and slope. Following the definition of Hult, Troy & Koseff (2011), the topographic characteristic slope was defined as $s = H_r/2\sigma$. The characteristic length of the ridge was defined as $L_s = 2\sigma$. Three topographic characteristic slopes were designed in the experiment, 0.20, 0.33 and 0.50, which are comparable to bathymetric slopes 0.07–0.5, where enhanced diapycnal diffusivities have been observed (Kunze & Sanford 1996; Toole *et al.* 1997). The densities of the two-layer stratified fluid remained constant, with density 1020 kg m^{-3}

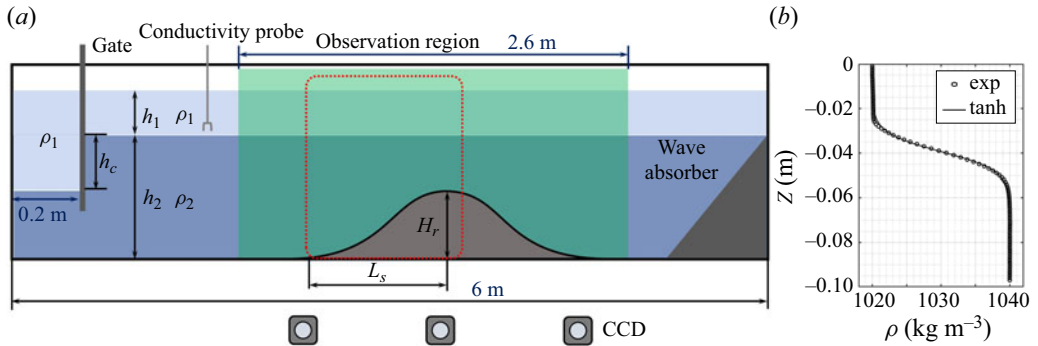


Figure 1. (a) Schematic diagram of the experimental set-up (not to scale). The fluids in the upper and lower layers are shown in light and dark blue, respectively. The green area and the red dotted box represent the particle image velocimetry observation regions for the large-region experiments and high-resolution experiments, respectively. The left-hand side is a wave-generating region by the standard lock-release method, and h_c is the collapse height. Here, H_r and L_s represent the height and characteristic length of the Gaussian ridge, respectively. The right-hand side is placed with a uniform slope for wave absorption (the slope is 0.33, with no porosity). (b) The measured density profile before the H2S1 run. The measured values are represented by circles, while the fitted results are represented by black lines.

in the upper layer (ρ_1) and 1040 kg m^{-3} in the lower layer (ρ_2). The depth of the upper layer (h_1) remained constant at 4 cm in all cases, and the lower layer (h_2) varied from 20 to 32 cm. The background stratification was measured with a conductivity probe before each experiment. The thickness of the interface $2h_t$ was obtained by fitting a hyperbolic tangent function to the measured profile ($\bar{\rho}(z) = \rho_0 - (\Delta\rho/2) \tanh((z - z_0)/h_t)$, where $\rho_0 = 1030 \text{ kg m}^{-3}$ is the reference density, $\Delta\rho = \rho_2 - \rho_1 = 20 \text{ kg m}^{-3}$, $z_0 = h_1$, and h_t is obtained by fitting). In this experiment, h_t ranged from 0.007 to 0.012 m. The width of the lock region was 20 cm, and the collapse height ranged from 4 to 24 cm (h_c), depending on the depth of the lower layer and the stratification conditions. The experimental conditions were a combination of different stratification conditions, topographic slopes and collapse heights, with a total of 60 experimental groups (table 2).

Particle image velocimetry (PIV) was used to measure the velocity field of the interaction between the ISWs and the Gaussian ridge. For large-region measurement experiments, three lasers (power 3 W, wavelength 532 nm) and three CCD cameras (Basler acA1920-155 μm) formed an experimental measuring range of up to 2.6 m (larger than the longest topography in this experiment), which could fully capture the incidence, shoaling, breaking, reflection and transmission processes of the ISWs. Images were taken at 50 Hz using 1920×1200 pixels for each CCD camera, to give spatial resolution 0.6 mm.

We used PIVlab (Thielicke 2014; Thielicke & Stamhuis 2014; Thielicke & Sonntag 2021), a MATLAB program package, to analyse the raw images. For cross-correlation algorithms, the multi-pass starting from the interrogation area 64×64 pixels, ending with a smaller interrogation area of 24×24 pixels with a 50% overlap, resulted in spatial resolution of the flow field at 7.2 mm (table 3). Consult Thielicke (2014) to estimate the magnitude of errors for the PIV analysis (detailed information is provided in § 1 of the supplementary material available at <https://doi.org/10.1017/jfm.2024.692>). The relative errors of the flow velocity are 0.8% and 3.8% for bias error and random error, respectively. According to Dalziel *et al.* (2007), the particle displacement caused by the index of refraction is a maximum of 1.1 mm (less than 2 pixels), based on the maximum buoyancy frequency in this experiment ($N^2 = 11 \text{ s}^{-2}$).

Breaking and energy distribution of ISWs over a ridge

Run	H (m)	s	h_c (cm)	a/h_1	Interaction type
H1S1	0.24	0.20	4, 8, 12, 16	0.48–1.62	F, PC, PC, PC
H1S2	0.24	0.33	4, 8, 12, 16	0.58–1.63	PC, PC, PC, PC
H1S3	0.24	0.50	4, 8, 12, 16*	0.52–1.61	PC, PC, PC, PC
H2S1	0.28	0.20	4, 8, 12, 16, 20	0.59–1.94	N, F, P, PC, PC
H2S2	0.28	0.33	4, 8, 12, 16, 20	0.54–1.93	N, T, P, PC, PC
H2S3	0.28	0.50	4, 8, 12, 16, 20	0.61–1.88	N, T, PC, PC, PC
H3S1	0.32	0.20	4, 8, 12, 16, 20	0.59–2.06	N, N, F, P, P
H3S2	0.32	0.33	4, 8, 12, 16, 20*	0.62–2.05	N, N, T, P, P
H3S3	0.32	0.50	4, 8, 12, 16, 20	0.65–2.01	N, N, T, P, P
H4S1	0.36	0.20	4, 8, 12, 16, 20, 24	0.61–2.29	N, N, N, N, T, P
H4S2	0.36	0.33	4, 8, 12, 16, 20, 24	0.65–2.30	N, N, N, T, P, P
H4S3	0.36	0.50	4, 8, 12, 16, 20, 24	0.64–2.36	N, N, N, T, P, P

Table 2. Experimental parameters, where H is the total water depth, s is the topographic slope, h_c is the collapse height, a is the incident wave amplitude, and h_1 is the depth of the upper layer. The letters in the last column indicate the interaction type (corresponding to h_c): N for no breaking, F for fission, T for transition P for plunging, PC for plunging–collapsing. The asterisks on h_c values indicate two additional cases of high-resolution experiments.

Experiment	Pixels	Frame rate (Hz)	Spatial resolution (mm)	Minimum interrogation area (pixels)	Velocity field resolution (mm)	Random error
Large region	1920 × 1200	50	0.6	24 × 24	7.2	3.8 %
High resolution	4096 × 3072	128	0.1	20 × 20	1.1	0.9 %

Table 3. Parameters of PIV analysis.

To assess the breaking and energy dissipation of ISWs on a ridge with greater precision, two additional cases of high-resolution experiments were conducted (as indicated by the asterisks in table 2, the experimental set-up was the same as that for the large-region experiment). However, the shooting area is limited to the upstream slope, as indicated by the red box in figure 1. Images were taken at 128 Hz using a 4096 × 3072 pixels CCD camera, to give spatial resolution 0.1 mm. The minimum interrogation area is 20 × 20 pixels with a 50 % overlap, resulting in the spatial resolution of the flow field being 1.1 mm. The relative errors of the flow velocity are 0.2 % and 0.9 % for bias error and random error, respectively (table 3).

2.2. Calculation method

The ISW stable propagation on a flat bottom prior to shoaling allowed identification of the waveform and calculation of basic physical quantities such as amplitude, wavelength and wave speed by schlieren (Wallace & Wilkinson 1988; Dalziel *et al.* 2007; Raffel 2015; Settles & Hargather 2017). The ISW propagation experiment without ridges was carried out to obtain wave parameters using background stripe schlieren (§ 2 of the supplementary material provides details on schlieren). The amplitude of the wave was determined by the maximum vertical displacement of the waveform, and the wavelength was determined by

the ratio of the integral of the wave profile to the amplitude:

$$L_w = \frac{1}{a} \int_{-\infty}^{+\infty} \eta(x) dx. \quad (2.1)$$

The wave speed (C_p) was determined by the distance of wave propagation within a given time. The incident amplitude, internal wave phase speed and characteristic wavelength were non-dimensionalized by the upper layer depth, linear phase speed (C_0) and harmonic mean of the water depth ($h_0 = h_1 h_2 / (h_1 + h_2)$), respectively.

Dimensionless parameters related to this experiment were determined by the wave parameters and the topography parameters, as shown in table 1. Dimensionless amplitudes include both weak and strong nonlinearities. The blockage parameter ranges from the weak interaction of waves that are almost unaffected to the strong interaction with wave breaking and mixing (Sveen *et al.* 2002; Chen 2009). The character of ISW breaking can be covered by Ir (Aghsaee *et al.* 2010; Sutherland *et al.* 2013). The experiments include scales of topographic length larger and smaller than the characteristic wavelength.

Kinetic energy is calculated as

$$E_k(x, z, t) = \frac{1}{2} \rho_0 [u(x, z, t)^2 + w(x, z, t)^2], \quad (2.2)$$

where ρ_0 is the reference density, and u and w are the horizontal velocity and vertical velocity retrieved from the PIV measurement, respectively.

The energy density is calculated by the vertical integral of the kinetic energy:

$$E_{kz}(x, t) = \int_0^H E_k(x, z, t) dz, \quad (2.3)$$

where $H = (h_1 + h_2)$ is the total water depth.

Following the method of Michallet & Ivey (1999), the kinetic and available potential energies are approximated for ISWs with small wave amplitudes (Bogucki & Garrett 1993); thus the total energy can be calculated as

$$E = 2C_p \int_{t_1}^{t_2} E_{kz}(X, t) dt. \quad (2.4)$$

The truncation of t_1 and t_2 is 1% of the maximum vertical integral of the energy, and X is a specific horizontal position. To avoid the influence of shoaling and breaking on the energy calculation, the incident wave energy was calculated before the interaction between the wave and ridge, and the reflected and transmitted wave energies were calculated after the ISW stabilized (Michallet & Ivey 1999). The calculated position of the incident wave and reflected wave is $X = -1.0$ m, and the transmitted wave is $X = 1.0$ m (we define the horizontal position of the top of the ridge as $X = 0$ m). This distance is half the length of the longest topography ($s = 0.2$, $\sigma = 0.4$, $X = \pm 2.5\sigma$), where the transmitted and reflected waves have developed into stable waveforms.

Since the 2-D velocity field can be obtained by the PIV system, the direct method is used to calculate the spatial distribution of the turbulent kinetic energy (TKE) dissipation rate. Based on the isotropic assumption, it can be calculated by the 2-D velocity field (Doron *et al.* 2001):

$$\varepsilon = 4\nu \left[\overline{\left(\frac{\partial u'}{\partial x}\right)^2} + \overline{\left(\frac{\partial w'}{\partial z}\right)^2} + \overline{\left(\frac{\partial u'}{\partial x} \frac{\partial w'}{\partial z}\right)} + \frac{3}{4} \overline{\left(\frac{\partial u'}{\partial z} + \frac{\partial w'}{\partial x}\right)^2} \right], \quad (2.5)$$

where u' and w' are the fluctuation velocities (the instantaneous velocity measured by PIV is used in this experiment). The kinematic viscosity coefficient is $\nu = 1.0 \times 10^{-6} \text{ m}^2 \text{ s}^{-1}$

(at laboratory temperature 20 °C). According to Cowen & Monismith (1997) and Liao *et al.* (2009), 99 % of the dissipation will be included with finite differencing if the PIV grid size is smaller than $5.5l_0$ (where $l_0 = (\nu^3/\varepsilon)^{1/4}$ is the Kolmogorov scale). Therefore, the high-resolution experiments are sufficient to estimate the TKE dissipation rate less than $8 \times 10^{-4} \text{ m}^2 \text{ s}^{-3}$. However, numerous factors can lead to anisotropic turbulence in the case of breaking interfacial waves. The estimates of dissipation obtained using various methods (dissipation from 2-D PIV, stereo-PIV, acoustic Doppler velocimeter data, and log-law data), parts of which rely on assumptions of isotropy, provide the same order-of-magnitude values (Zahedi 2021).

3. Results

3.1. Evolution process

In this subsection, a series of dynamic processes, such as shoaling, breaking, transmission and reflection, as well as the evolution of wave energy, are presented through several sets of typical experiments.

The superposition of the vorticity and flow fields is presented in figure 2 to provide a detailed view of the structure of the breaking process. As shown in figure 2, the process of interaction of plunging–collapsing breaking can be divided into the following four stages (sketches of each stage are presented in Appendix A).

- (1) In figure 2(a), the wave trough propagates to the toe of the slope, at which time the bulk of the wave starts to contact the topography. A vorticity structure forms at the interface due to the mode-1 velocity field of the depressed ISW.
- (2) Due to topographic modulation, the propagation speed of the trailing edge of the wave is greater than that of the wave trough, making the trailing edge steeper. The maximum horizontal velocity of the upper layer moves to the trailing edge of the wave. The waveform on the left-hand side of the ridge is parallel to the topography, the downslope velocity of the lower layer increases, and part of the wave is transmitted through the top of the ridge (figure 2b).
- (3) The ISW becomes unstable, and the velocity of the water particle on the trailing edge of the wave exceeds the wave speed (Vlasenko & Hutter 2002; Lien *et al.* 2014), resulting in convective instability and flow separation at the benthic boundary layers in the adverse pressure gradient region (red arrow in figure 2c). The two types of instability processes generate distinct positive vorticities above and below the pycnocline.
- (4) In figures 2(d,e), the ISW breaks, and the vortices resulting from the initial instability split into smaller scales, generating strong turbulent mixing on the ridge. Simultaneously, generated reflected waves (figure 2e, positive vorticity, $x = -0.6 \text{ m}$) and transmitted waves (figure 2d, negative vorticity, $x = 0.7 \text{ m}$) have left the topography. The transmitted wave is followed by a significant dispersive wave tail, whereas the reflected wave is not. In the weak interaction with a small blockage parameter, ISWs do not break, only the waveform is modulated by the topography, and no reflected wave generation occurs.

For ISWs breaking, not only convective instability and bottom boundary instability are present, but also Kelvin–Helmholtz billows generated by shear instability can be identified via high-resolution experiments (figure 3). During the upwelling of the fluid mass induced by plunging in plunging–collapsing breaking, strong flow still exists in the lower layer. Consequently, billows induced by strong shear are continuously generated

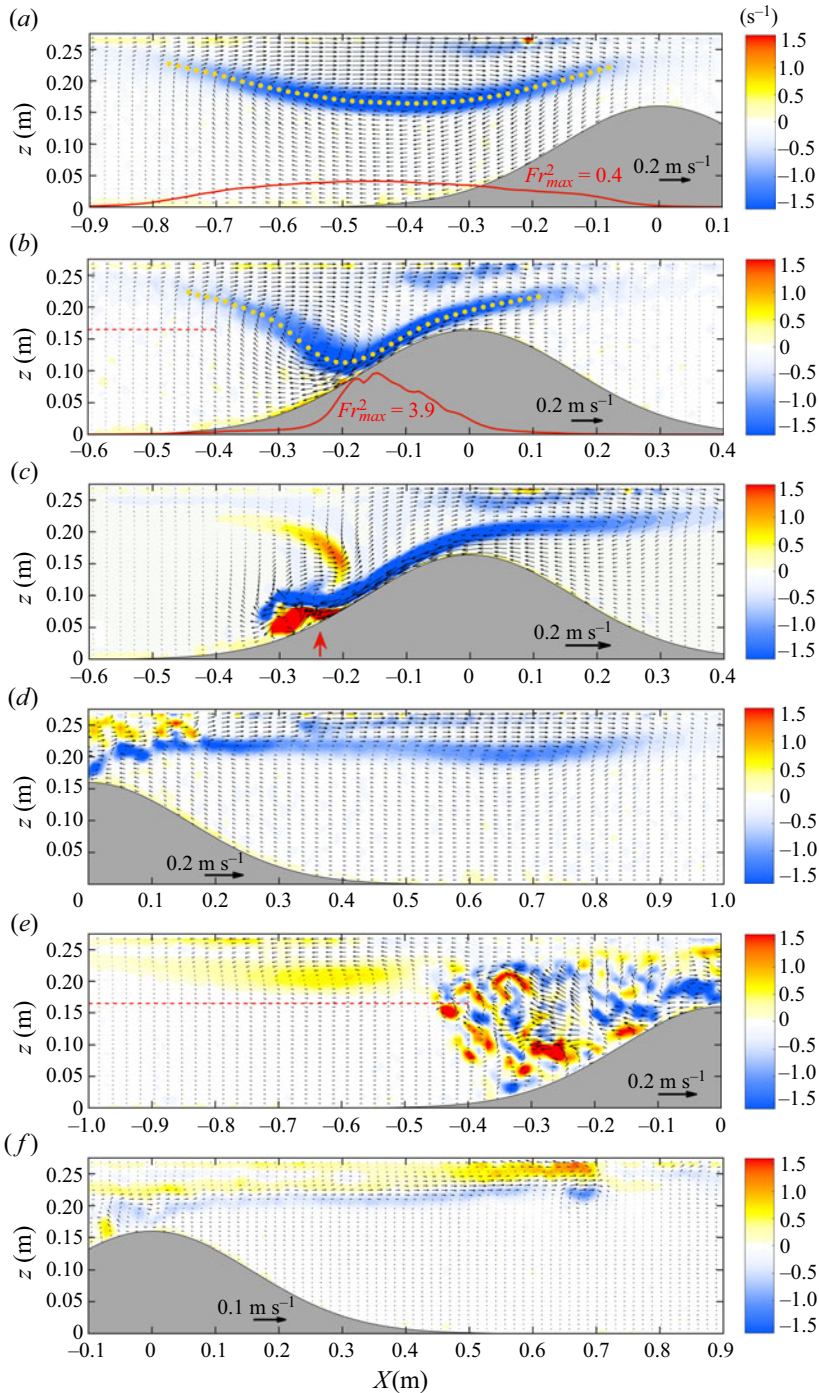


Figure 2. Evolution of the interaction between ISWs and topography. The image is a superposition of the vorticity and flow fields for values of t (a) 0 s, (b) 3.0 s, (c) 5.0 s, (d) 11.0 s, (e) 11.0 s, (f) 28.2 s. The experimental conditions are as follows: the water depth is $H = 0.28$ m, the slope is $s = 0.50$, and the incident wave amplitude is $a = 0.075$ m. In (a) and (b), the yellow dots represent the waveforms identified by the vertical position of the extremes of the velocity shear in each column, and the red lines represent the composite Froude number. The red dashed lines in (b) and (e) represent the depth of the incident amplitude. The red arrow in (c) indicates the adverse pressure gradient region.

Breaking and energy distribution of ISWs over a ridge

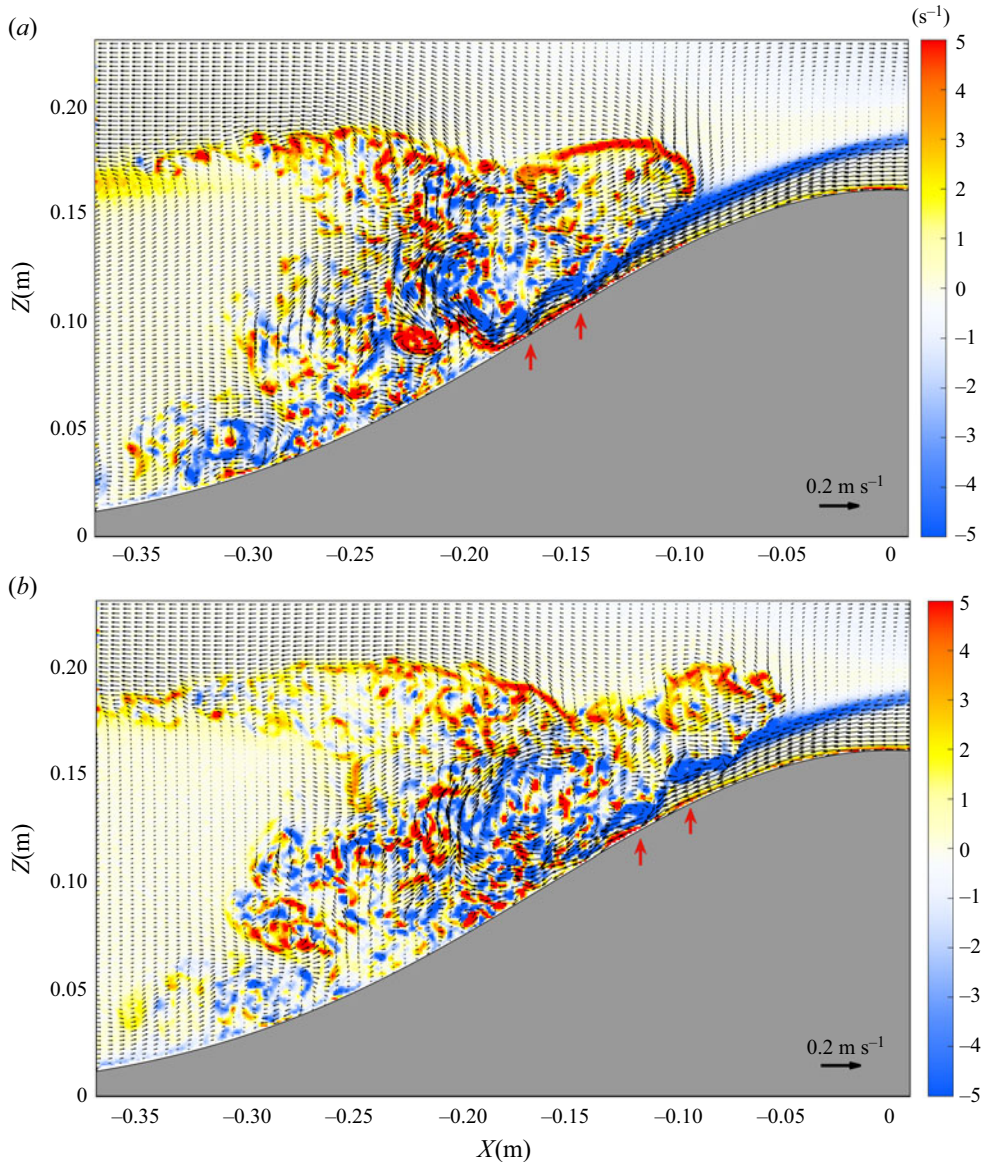


Figure 3. The evolution vorticity field of plunging–collapsing breaking in high-resolution experiments, $H = 0.24$ m, $s = 0.50$ and $a = 0.064$ m, for (a) $t = 13.7$ s, and (b) $t = 14.9$ s. Red arrows indicate Kelvin–Helmholtz billows.

initially as 2-D vortices and subsequently split into three-dimensional (3-D) states (red arrows in figure 3). In this instance, the billow was generated at a location different from that in previous observations, with the billow appearing only at the trailing edge of the wave (Moum *et al.* 2003; Chang *et al.* 2021). For ISWs, the breaking threshold is $L_x/2L_w = 0.86$, where L_x is the horizontal length of the region in which the Richardson number is less than 0.25 (Fructus *et al.* 2009; Barad & Fringer 2010; Carr, King & Dritschel 2011). The numerical simulation of Xu, Stastna & Deepwell (2019) indicated that when $L_x/2L_w \approx 0.88$, the shear instability occurs spontaneously, without any externally

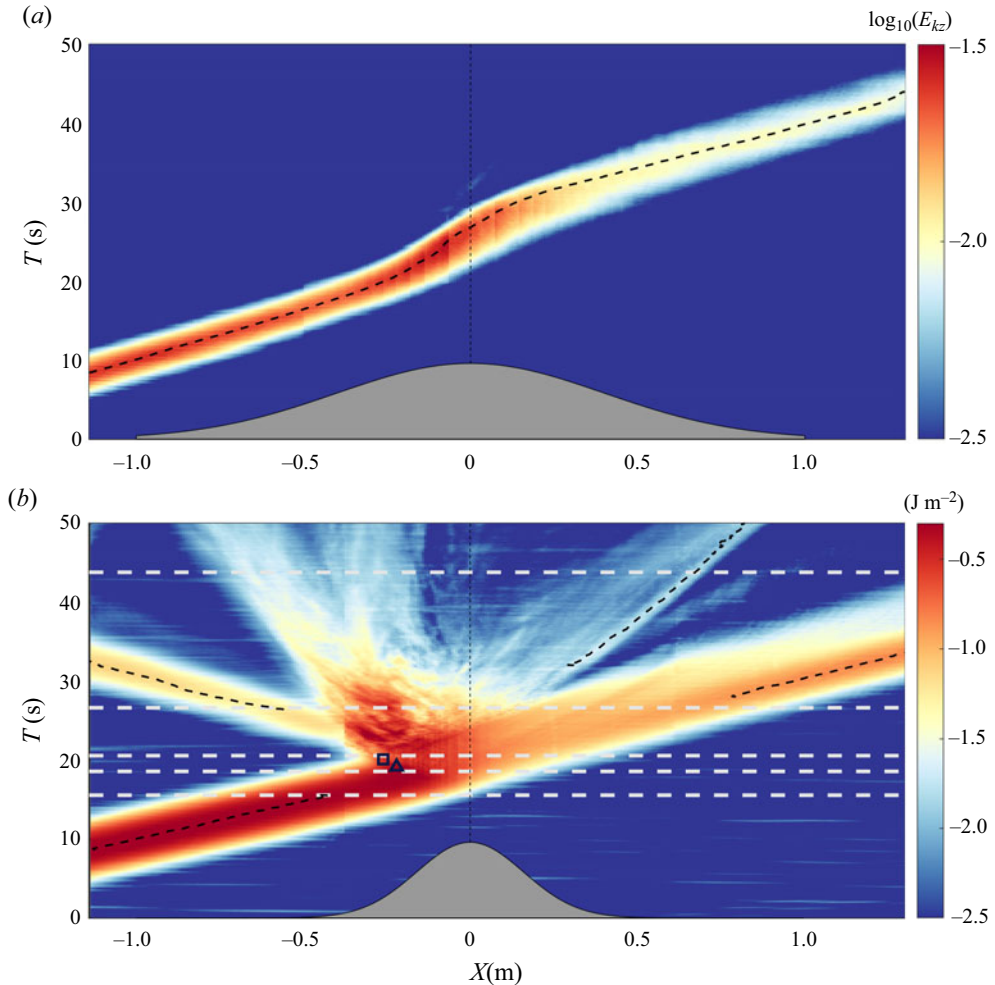


Figure 4. Time series showing the vertical integral of kinetic energy along the length of the observation region. (a) The water depth is $H = 0.24$ m, the slope is $s = 0.20$, and the incident wave amplitude is $a = 0.019$ m. (b) The water depth is $H = 0.28$ m, the slope is $s = 0.50$, and the incident wave amplitude is $a = 0.075$ m. The black dashed lines represent the maximum value of the energy density of different wave rays. The white dashed lines correspond to the five moments in figure 2. The square and triangle in (b) correspond to the start times (horizontal coordinates indicate the breaking position) of plunging breaking and collapsing breaking, respectively.

imposed physical noise. In the absence of direct density measurements in this experiment, visual vortex development was relied upon for this part of the analysis of the process of shear instability and Kelvin–Helmholtz billows. According to the definition of Carr *et al.* (2017), the dimensionless billow wavelength in figure 3(b) is $\lambda_b/2h_t = 2.0$ ($h_t = 0.8$ cm), and the dimensionless vertical extent of the billow at $x = -0.09$ m is $L_b/2h_t = 0.73$. Both of these scales are significantly smaller than the billow at the trailing edge of the wave as shown in Carr *et al.* (2017, tables 2 and 3). This may be due to the wavelength of the fastest growing wave of disturbance being determined by velocity shear and stratification (Xu 2015).

Figure 4 shows the evolution of ISWs over the ridge by using the vertical integral of the kinetic energy (2.3). In figure 4(a), with a small incident amplitude, the ISW will not break

when it passes through the topography, but its propagation speed is clearly modulated by the topography. The wave speed slows at the top of the ridge, and gradually returns to a constant speed after passing over the ridge. As the lower water depth at the ridge becomes shallower, the shear at the interface is enhanced. The energy is decreased in the laminar flow by the viscosity, as there are no instability processes during the evolution. This leads to a significant decrease in the energy density after the wave passes over the ridge. In this case, following the usual definition for stratified shear flows, a Reynolds number is introduced as $Re = \Delta u h_i / 2\nu = 88$, where Δu is the velocity jump across the pycnocline when the wave trough passes over the top of the ridge. For $Re \leq 100$, viscosity reduces the growth rate and damps the high wavenumber perturbations (Hogg & Ivey 2003; Fructus *et al.* 2009).

The experimental conditions in figure 4(b) are the same as in figure 2. The white dashed lines in figure 4(b) correspond to the five moments in figure 2, and the black dashed lines represent the positions of the maximum energy density of different wave rays. The ISW will be broken when interacting strongly with the ridge, generating transmitted and reflected waves, accompanied by mode-2 ISW generation. The wave speed was calculated by the slope of the maximum energy density curve, and the incident wave speed was 0.104 m s^{-1} , the transmitted wave speed was 0.093 m s^{-1} , and the reflected wave speed was 0.091 m s^{-1} . The propagation speed of the mode-2 wave measured in the experiment was 0.0283 m s^{-1} . The three-layer model of Yang *et al.* (2010) was used to evaluate the propagation speed of mode-2 solitary waves. Taking the middle layer thickness as 2.4 cm ($2h_i$), the theoretical calculation result was 0.0299 m s^{-1} , which was consistent with the experimental result. The energy of this mode-2 ISW (calculated by multiplying the kinetic energy integral for $x = 0.63\text{--}0.73 \text{ m}$ in figure 2(f) by 2) is 0.42 % of the incident wave energy.

3.2. *Breaking types*

The ISW shoaling on the slope has two typical characteristics: (1) the trailing edge of the wave becomes steeper; (2) the lower layer fluid flows downwards and increases in velocity under the compression of the wave and topography (figure 2b) (La Forgia, Adduce & Falcini 2018). As shown in figures 2(a–c), the cumulative effect of nonlinearity in a shoaling ISW leads to a steepening and overturning of the rear wave face (Vlasenko & Hutter 2002). Because the ridge does not coincide with the pycnocline, the varying rate of the stratification nonlinear coefficient is determined by a combination of ridge slope and height. Fluid can be replenished from the other side of the ridge during shoaling (the height of the ridge can adjust the width of the lower layer channel), making the velocity of the lower fluid layer much higher than that of shoaling on the uniform slopes. Therefore, the ridge height and slope are two important parameters in controlling the breaking type.

The shoaling of ISWs on uniform slopes is regulated by the wave slope and the topographic slope, resulting in plunging breaking, collapsing breaking, surging breaking, plunging–collapsing breaking and fission (Boegman *et al.* 2005; Aghsaei *et al.* 2010; Sutherland *et al.* 2013; Nakayama *et al.* 2019). Given that breaking on uniform slopes has been defined clearly, the type of breaking on ridges is classified in terms of the dynamic processes of shoaling on uniform slopes. However, different from the uniform slope, the wave–ridge interaction not only has shoaling breaking and reflection, but also has a transmission process when passing through the ridge (Sveen *et al.* 2002; Chen 2009; Sutherland *et al.* 2015). The interaction types were classified into the following five categories by analysing the experimental data (figure 5, plus sketches in § 3 of the supplementary material).

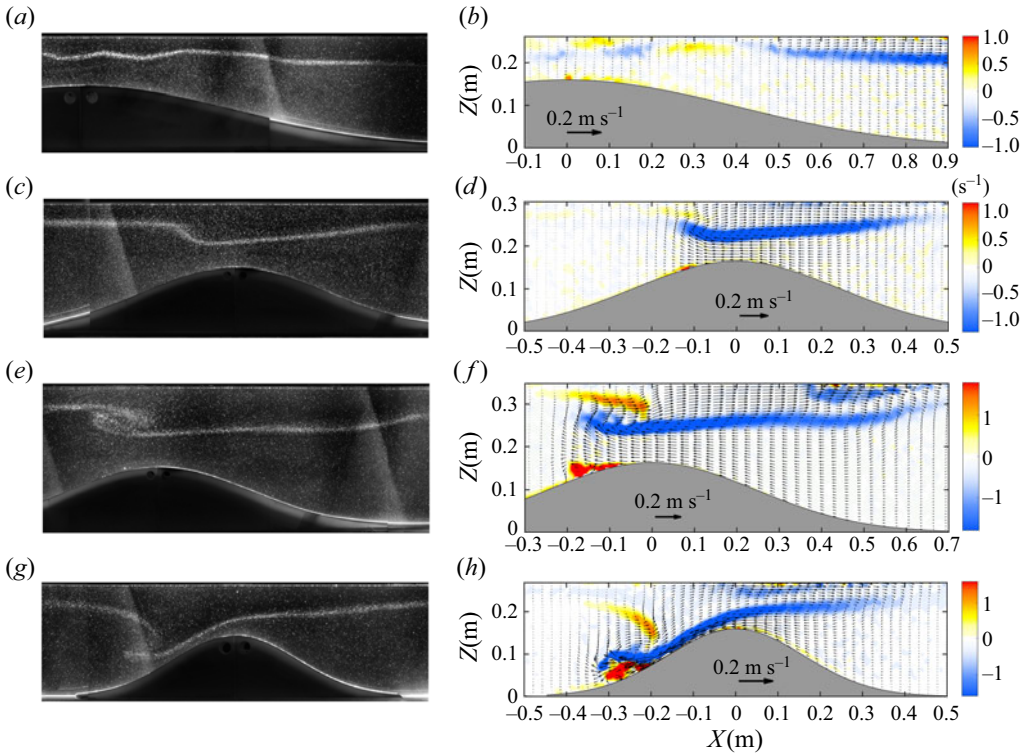


Figure 5. Different types of ISWs interact with ridges: (a,b) fission, (c,d) transition, (e,f) plunging breaking, and (g,h) plunging–collapsing breaking. The raw PIV images are shown in (a,c,e,g), with corresponding superimposed vorticity and flow fields in (b,d,f,h). Experimental conditions: (a) $h_1 = 0.04$ m, $h_2 = 0.24$ m, $s = 0.20$, $a = 0.040$ m, $\zeta = 0.65$, $Ir = 0.65$; (c) $h_1 = 0.04$ m, $h_2 = 0.28$ m, $s = 0.33$, $a = 0.055$ m, $\zeta = 0.58$, $Ir = 0.95$; (e) $h_1 = 0.04$ m, $h_2 = 0.32$ m, $s = 0.33$, $a = 0.092$ m, $\zeta = 0.63$, $Ir = 0.82$; (g) $h_1 = 0.04$ m, $h_2 = 0.24$ m, $s = 0.50$, $a = 0.075$ m, $\zeta = 0.91$, $Ir = 1.30$.

- (1) Weak interaction. When $\zeta < 0.5$, the waveform is almost unaffected by the ridge or is slightly deformed.
- (2) Fission. This occurs when both the slope and the incident amplitude are smaller. Significant fluctuations at the top of the ridge (figure 5a) cause alternating positive and negative vorticity at the interface (figure 5b); meanwhile, the bulk of the wave energy is transmitted past the ridge.
- (3) Transition. There is a transition state between ISW breaking and no breaking. During the shoaling process, the trailing edge of the wave becomes steeper and almost perpendicular to the horizontal direction. However, simultaneously, the tail of the wave is located close to the top of the ridge (figure 5c), and the cumulative effect of nonlinearity no longer continues, so the trailing edge of the wave does not reach an overturned state when it passes over the ridge topography. In this state, if the incident amplitude or the topographic slope is increased, breaking will occur. This process does not occur in the interaction of ISWs with uniform slopes, where the continued cumulative effect of nonlinearity will cause convective instability (Boegman *et al.* 2005; Sutherland *et al.* 2013).
- (4) Plunging. The rear face of the wave overturns, resulting in convective instability in the horizontal direction, leading to plunging breaking. This breaking process is dominated by the dynamics on the pycnocline and is independent of the benthic

boundary dynamics. The vortex at the top of the ridge represents the flow separation of the lower layer fluid around the topography without encountering the pycnocline.

- (5) **Plunging–collapsing.** The rear face of the wave overturns, and the separation bubble is generated on the ridge, resulting in plunging–collapsing breaking, similar to the same breaking type on a uniform slope (Aghsaei *et al.* 2010; Sutherland *et al.* 2013) and the strong interaction of the mode-2 ISW with a narrow ridge (Deepwell *et al.* 2017). In this condition, $\zeta > 0.75$, and the maximum interfacial vertical displacement of the ISW increases significantly. The generated vortices in the benthic boundary layer and the rear face of the wave cause global breaking and mixing on the left-hand side of the ridge.

Both plunging and plunging–collapsing breaking result in the dissipation of significant wave energy over the ridge. The analysis of the high-resolution flow field data to show the distribution of the TKE dissipation rate characteristics of wave breaking has greater significance. In figures 6(e–h), for plunging breaking, the high-value region of dissipation is generated primarily by velocity shear and wave breaking at the pycnocline in the interior, as well as by instability processes at the benthic boundary layer. A straightforward spatial delineation of the high-value dissipative areas can be identified within these two regions. Figures 6(e–g) correspond to the three peaks of the space integration of the ε time series in figure 6(h), respectively (represented by triangles). The initial peak is indicative of the generation of vortices at the bottom boundary, with dissipation originating primarily from this region, which accounts for 67% of the space. By the second peak, the vortices generated at the bottom boundary broke into smaller vortex structures due to the instability in 3-D effects. The convection-induced plunging breaking, on the other hand, is sufficiently developed so that the dissipation percentage near the pycnocline is larger than that at the bottom boundary. (Due to the limitation of the observation region, some of the processes are already out of the field of view, which will underestimate the dissipation percentage near the pycnocline.) The third peak represents the maximum moment of dissipation for plunging breaking. Initially generated 2-D vortices are fully transformed into complex 3-D structures, with the dissipation percentage induced by the bottom boundary being 18% greater than that near the pycnocline upstream of the ridge. In general, the dissipation percentage of the interior is lower than that of the bottom boundary during plunging breaking. This finding is similar to the results of Arthur & Fringer (2014), who found that the ratio of dissipation in the interior and bottom boundary is approximately 1 : 2 for the ISW breaking on a uniform slope.

For plunging–collapsing breaking, the dissipation at the pycnocline and the bottom boundary are superimposed on each other due to the ISW directly impinging upon the ridge. The high-value region is mainly distributed upstream of the ridge. Figures 6(a–c) correspond to the three typical moments of the space integration of ε in figure 6(d), respectively. In figure 6(a), the dissipation is attributed primarily to vortices generated by collapsing breaking (purple dashed rectangle) and enhanced shear (blue dashed rectangle). Subsequently, in figure 6(b), the dissipation due to collapsing breaking decreases, while the dissipation due to plunging breaking increases rapidly, resulting in a nearly one-fold increase in the total dissipation rate within 1.7 s (figure 6(d), 10.5–12.2 s). After the peak, the upwelling of the fluid mass induced by plunging ($x = -0.2$ to -0.1) maintains dissipation at a high value (figure 6c). The rate of increase in the dissipation rate of plunging–collapsing breaking is much greater than that of plunging breaking because the dissipation in plunging–collapsing breaking is caused by the sudden release of available potential energy accumulated upstream (figures 6a,b), whereas the dissipation in

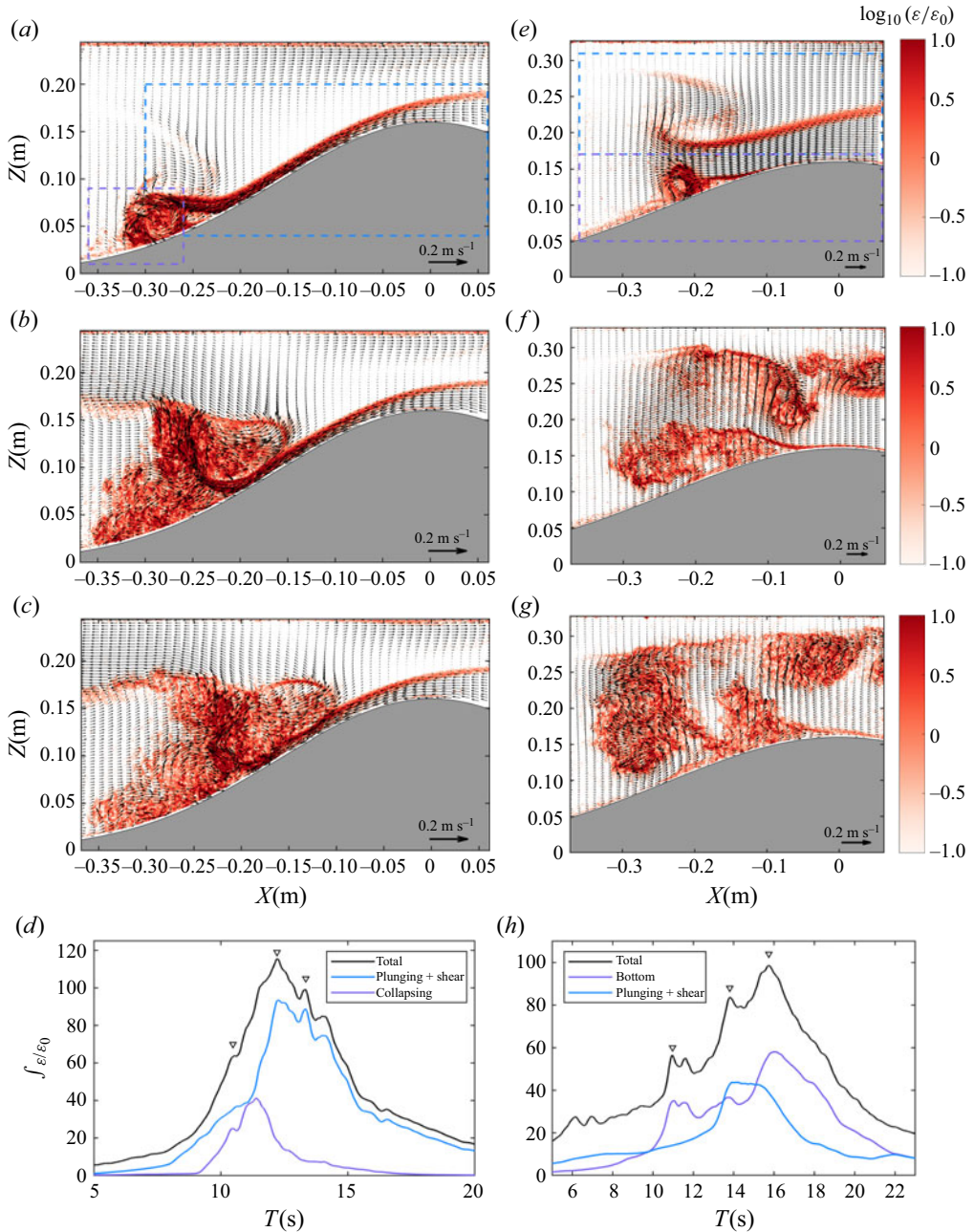


Figure 6. The evolution of the TKE dissipation rate of (a–d) plunging–collapsing breaking, $H = 0.24$ m, $s = 0.50$, $a = 0.064$ m, and (e–h) plunging breaking, $H = 0.32$ m, $s = 0.33$, $a = 0.082$ m, for values of t (a) 10.5 s, (b) 12.2 s, (c) 13.3 s, (e) 11.0 s, (f) 13.8 s, (g) 15.7 s. (a–c, e–g) The spatial distribution of the TKE dissipation rate, which is dimensionless by the mean dissipation at the pycnocline of the wave trough before ISW breaking ($\epsilon_0 = 1.4 \times 10^{-4} \text{ m}^2 \text{ s}^3$ in plunging–collapsing breaking, and $\epsilon_0 = 1.2 \times 10^{-4} \text{ m}^2 \text{ s}^3$ in plunging breaking). (d, h) The black line is the time series of the spatial integration of the TKE dissipation rate, and the three triangles correspond to the three moments in (a–c, e–g). The purple and blue lines correspond to the time series of the spatial integration of TKE dissipation rate points in the matching coloured dashed boxes in (a) and (e), respectively. The box in (a) is fixed in time, while that in (e) moves with the flow.

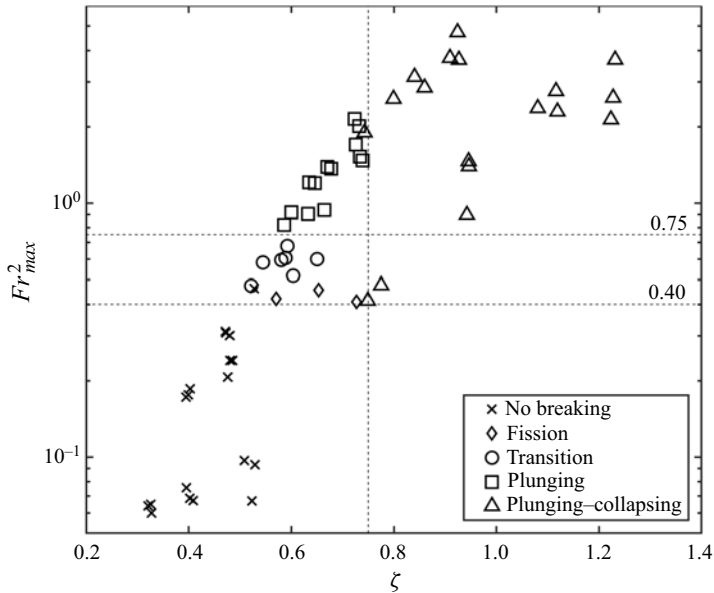


Figure 7. Types of wave–ridge interactions in relation to ζ and the maximum Froude number. The two horizontal dashed lines correspond to $Fr_{max}^2 = 0.40$ and $Fr_{max}^2 = 0.75$. The vertical dashed line corresponds to $\zeta = 0.75$. Crosses indicate no breaking, diamonds indicate fission, hollow circles indicate transition state, squares indicate plunging breaking, and triangles indicate plunging–collapsing breaking.

plunging breaking is attributed mainly to relatively slow overturning and bottom boundary instability.

3.3. Breaking criterion

The strength and breaking type of the wave–ridge interaction depends on the topography and wave parameters. Different interactions and breaking types are accompanied by different turbulent mixing and energy dissipation. In the experiment, the dimensionless parameters controlling ISW breaking were varied by adjusting the topographic slope, the stratification condition and the internal wave amplitude, totaling 60 sets of experimental data. This subsection considers the effect of both ridge height (introducing the blockage parameter) and the variation in the flow field during wave shoaling (introducing the Froude number) on ISW breaking. The effects of considering both ridge height and slope will be discussed in § 4.

Figure 7 considers the blockage parameter. When $\zeta < 0.5$, the ISW is almost unaffected by the ridge, and no breaking occurs. When the blockage parameter is sufficiently large ($\zeta > 0.75$), only plunging–collapsing breaking occurs on the ridge. Four different interaction types may occur within the range $0.5 < \zeta < 0.75$.

Convective instability appears in both plunging breaking and plunging–collapsing breaking (figures 5*f,h*), which resembles field observations as shown in Lien *et al.* (2014, their figure 3) and Chang *et al.* (2021, their figure 2), and previous numerical simulations in the shoaling of internal waves (Lamb 2002, 2003; Lamb & Farmer 2011; Rivera-Rosario *et al.* 2020, 2022). The convection in this experiment is generally stronger than the field observations because the topographic slope of the ocean is milder and the internal waves have sufficient time to adjust waveforms. In field observations, convective breaking is

often examined by the along-wave current velocity exceeding the wave speed. Laboratory measurements provide the spatiotemporal structure of the velocity, and the character of the flow regimes of wave shoaling can be characterized by the composite Froude number (Maderich *et al.* 2010):

$$Fr^2 = \frac{U_1^2}{g'(h_1 - \eta)} + \frac{U_2^2}{g'(h_2 + \eta)}, \quad (3.1)$$

where U_1 and U_2 are the average horizontal velocities in the upper and lower layers, respectively, and g' is the reduced gravity. The maximum Froude number (Fr_{max}) increases significantly during the wave–ridge interaction (figures 2*a,b*), providing a clear distinction between the different interaction types (figure 7). In the case of no breaking, $Fr_{max}^2 < 0.40$. For fission and transition, $0.40 < Fr_{max}^2 < 0.75$, $\zeta < 0.75$. For plunging breaking, $Fr_{max}^2 > 0.75$. Plunging–collapsing breaking occurs for $\zeta > 0.75$ and $Fr_{max}^2 > 0.40$.

3.4. Breaking time scale

Two kinds of dynamic processes lead to the breaking of the ISW interaction with the ridge: onshore overturning of the trailing edge (plunging breaking), and flow separation on the topography (collapsing breaking). To evaluate the breaking process, the trough of the wave reaching the toe of the slope ($X = -L_s$) was taken as the starting point of time, and two types of time scales were calculated. The time needed for plunging breaking (T_p) is governed by the time when positive vorticity appears in the wave tail. The time needed for collapsing breaking (T_c) is governed by the time when the separated bubble contacts the pycnocline, leading to instability (Aghsaee *et al.* 2010).

Figure 8(*a*) shows the time scale of plunging breaking, which is dimensionless through the time (L_s/C_p) of the internal wave propagating over the topographic scale (where L_s is the horizontal distance from the toe to the top of the ridge) without the topography. Compared to the time of the internal wave passing through the topographic scale, the larger the blockage parameter or the smaller the Iribarren number, the earlier the trailing edge overturning leads to breaking. Figure 8(*b*) shows the ratio of plunging breaking and collapsing breaking time scales (T_p/T_c), revealing that the larger ζ and Ir , the earlier collapsing breaking occurs. The experimental results show that most collapsing breaking occurs earlier than plunging breaking. If plunging breaking occurs too early, then the maximum interfacial descent will dampen and be located far from the ridge, which is not sufficient to cause collapsing breaking. In figure 8, there is a monotonic relationship between dimensionless T_p and T_c , and Ir and ζ , indicating that the time scale of breaking can be predicted by an empirical formula based on Ir and ζ (see § 4 of the supplementary material).

4. Discussion

In § 3, the basic characteristics and energetics of ISWs passing over ridges are described by means of the velocity field in a large region, and the types of interaction are classified. The dynamic mechanisms of different breaking types are studied, and a preliminary analysis of the breaking criterion of the wave–ridge interaction is presented based on the Froude number and the blockage parameter.

Furthermore, a clear understanding of the energy distribution of wave–ridge interactions allows for a better evaluation of the oceanic energy budget and serves parametrization. Hence previous studies have defined different parameters to examine the energy

Breaking and energy distribution of ISWs over a ridge

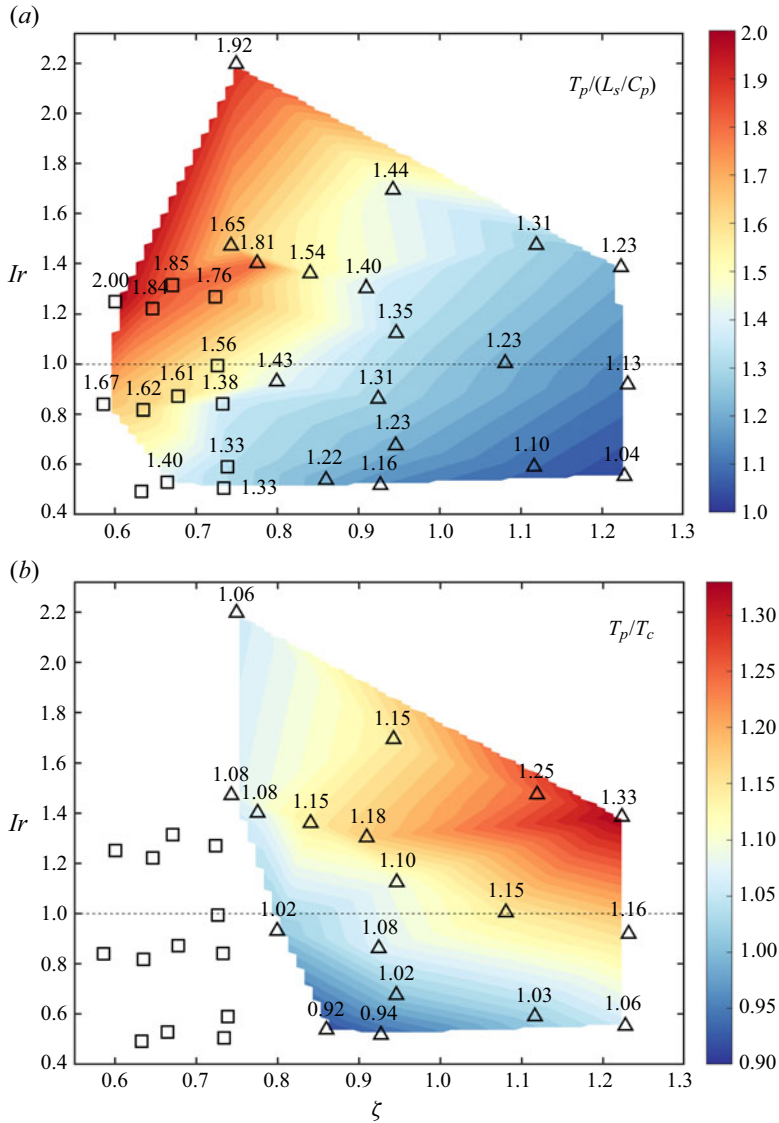


Figure 8. (a) The dimensionless plunging breaking time scale; the numbers on the triangles and squares are $T_p/(L_s/C_p)$. (b) Ratio of the plunging breaking time scale to the collapsing breaking time scale; the numbers on the triangles are T_p/T_c . The legend is the same as in figure 7, with the background colour obtained by interpolation.

distribution of the interaction of ISWs with the ridge, considering the effect of ridge height – Chen (2009) by means of the blockage parameter, Zhu *et al.* (2016) using the empirical formula for multiplying the degree of blocking with the nonlinear factor ($B_m = B(a/h_1)^{\alpha_0}$, $B = H_r/h_2$, α_0 is a constant), and Sutherland *et al.* (2015) with the exponential fitting curve based on the critical amplitude ($A_{c0} \equiv \frac{1}{2}(h_2 - H_r - h_1) + \sqrt{h_1(h_2 - H_r)}$) – to evaluate the energy distribution. However, none of these methods accounts for the effect of the topographic slope, so the data points are scattered when calculating the energy distribution for this experiment (see § 5 of the supplementary material). Moreover, there is regional overlap when using the blockage parameter to separate breaking types. Therefore, it is

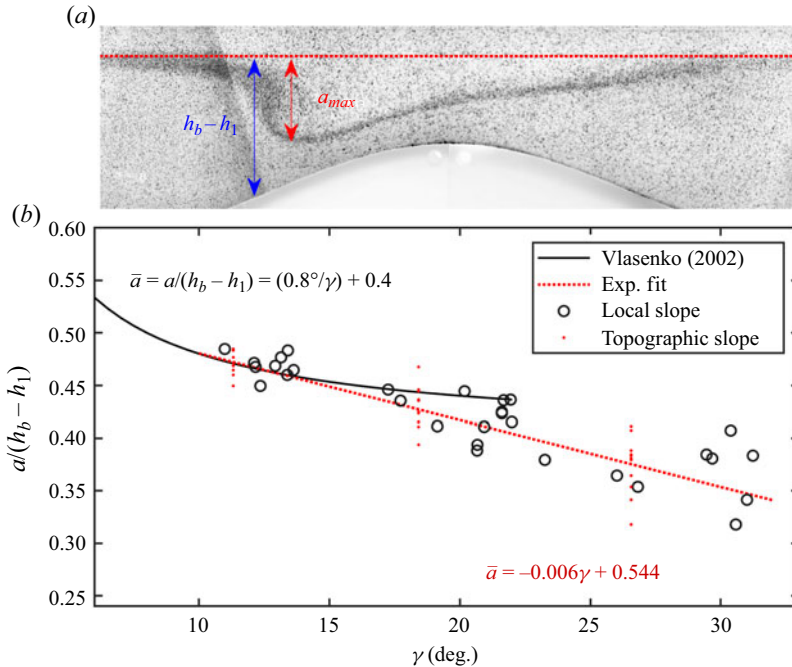


Figure 9. (a) Snapshot of the PIV image (in false colour); the blue arrows show the depth of the lower fluid layer at the location of breaking, and the red arrows show the maximum interface vertical displacement. (b) Breaking depth criterion of plunging and plunging–collapsing. The black line is the fitting result of Vlasenko & Hutter (2002). The horizontal coordinates of the three sets of red dots ($\gamma = 11.3^\circ$, 18.4° and 26.6°) correspond to the characteristic slopes of the three ridges in this experiment. The horizontal coordinates of the black circles correspond to the local topographic slope at the breaking position. The red dashed line is a linear fit to the red dots.

necessary to introduce a new breaking criterion to characterize the degree of interaction to diagnose the energy distribution and to distinguish the type of breaking.

Note that the amplitude of the ISW changes during shoaling, which affects the degree of wave–ridge interaction. Therefore, the combined effects of ridge height and slope are accounted for to introduce an important parameter that represents the effect of wave shoaling: the maximum interface descent (a_{max}). A prediction scheme for a_{max} is given in § 4.1. A new breaking criterion is derived based on a_{max} , namely the modified blockage parameter, which is used to analyse the type of breaking and energy distribution in §§ 4.2 and 4.3, respectively.

4.1. The maximum interface descent

To examine the maximum interface descent of ISWs shoaling on the slope, Sutherland *et al.* (2013) assumed that the area of the incident wave was equal to the critical state before breaking (1.3). For ISWs breaking over the ridge, the area equation can also be established. Assuming that the rear face of the wave is perpendicular to the horizontal direction before breaking, the waveform on the left-hand side of the ridge is consistent with the topographic slope (figure 9a), and the transmitted wave slope is consistent with the incident wave slope. The critical waveform of the ISW before breaking is approximated as the quadrilateral in figure 10.

Breaking and energy distribution of ISWs over a ridge

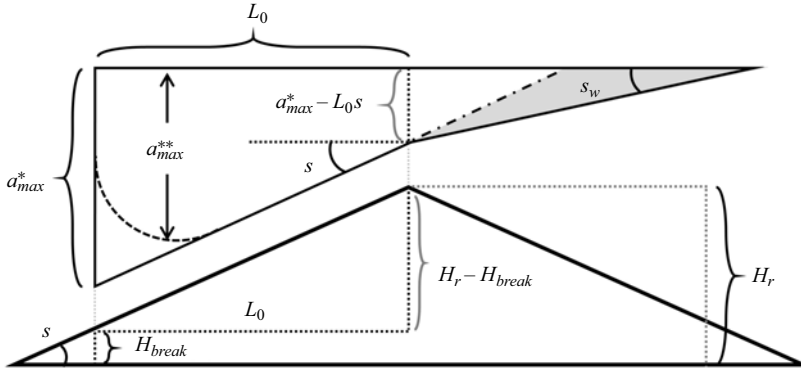


Figure 10. An approximate diagram of the waveform before the breaking of the ISW on the ridge, where a_{max}^* is the maximum interface descent, L_0 is the horizontal distance between the breaking location and the top of the ridge, s and s_w are the topographic slope and wave slope, H_r is the topographic height, and H_{break} is the topographic height at the breaking location. The dashed curve is a portion of the inscribed circle of the triangle enclosed by the left-hand waveform and the chain line, and a_{max}^{**} is the modified maximum interface descent.

The incident wave parameters and ridge parameters can be obtained before the wave–ridge interaction, and the breaking location can be calculated with reference to the work of Vlasenko & Hutter (2002) (see (1.2)). As shown in figure 9(b), the depth of breaking in this experiment (red dots) is consistent with the ocean-scale numerical simulations for seabed topographic slopes less than 20° (black line).

The horizontal distance between the breaking location and the top of the ridge (L_0) can be calculated from the prediction results in figure 9(b):

$$L_0 = \frac{H_r - H_{break}}{s}, \quad (4.1)$$

$$H_{break} = H - h_b, \quad (4.2)$$

where H_{break} is the topographic height at the breaking location, and h_b , the critical depth of breaking, can be calculated using (1.2) (equating the left-hand side to the right-hand side, $a/(h_b - h_m) = 0.8^\circ/\gamma + 0.4$). Also, L_0 should be obtained by integration if the topographic slope changes greatly (Sutherland *et al.* 2013). The minimum value on the right-hand side of (1.2) is 0.4. However, the calculations in this experiment indicate that the result will be less than 0.4 as the slope of the topography increases. Therefore, (4.2) can be replaced by the fitting results in figure 9 when the topographic slope is greater than 20° .

Given the incident wave area ($S_{ISW} = aL_w$), incident wave slope (s_w), topographic slope and breaking location, the equation can be established based on the assumption that the area of the incident wave was equal to the critical state before breaking to obtain the predictions of maximum interface descent (a_{max}^*):

$$S_{ISW} = \frac{(a_{max}^*)^2}{2s} + \left(\frac{a_{max}^* - L_0s}{2} \right) \left(\frac{a_{max}^* - L_0s}{s_w} - \frac{a_{max}^* - L_0s}{s} \right). \quad (4.3)$$

The right-hand side of (4.3) corresponds to the area of the quadrilateral in figure 10. The first and second terms represent the areas of the white and grey triangles, respectively.

Equation (1.3) is valid on a uniform slope that intersects the pycnocline. However, due to the transmission process of ISWs passing over the ridge, not all of the wave energy

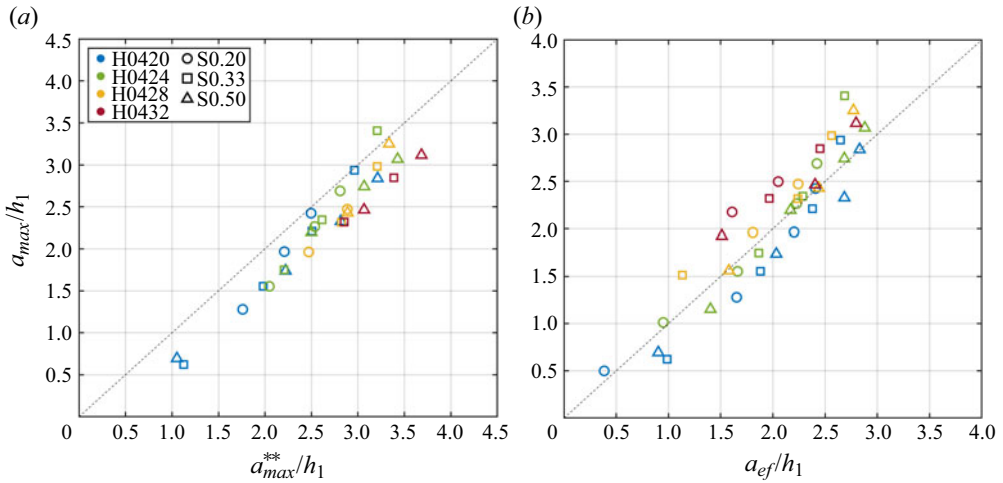


Figure 11. Maximum interface descent predictions versus measurements. (a) Predictions obtained by assuming that the incident waveform area and the area before breaking are equal. (b) Results predicted by the empirical formula. Blue, green, yellow and red indicate the upper and lower water depth ratios 4 : 20, 4 : 24, 4 : 28 and 4 : 32 (the units are in cm), respectively. Triangles, squares and circles indicate topographic slopes 0.50, 0.33 and 0.20, respectively.

accumulates in front of the ridge, as illustrated in figure 10, where the grey shaded region is behind the ridge (relative to the direction of wave propagation), so the amplitude growth is less than the uniform slope. The left-hand side and the first term on the right-hand side in (4.3) ($S_{ISW} = (a_{max}^*)^2/2s$) are consistent with (1.3), while the second term on the right-hand side, as an additional term, represents the difference between predictions on ridges and slopes. Consequently, the prediction scheme for the slope cannot be used to estimate the maximum interface descent on the ridge. (In this experiment, the wave slope is smaller than the topographic slope, which would increase the prediction.) Shifting (4.3), we obtain

$$\frac{1}{2s_w} (a_{max}^*)^2 + \left(\frac{L_0s}{s} - \frac{L_0s}{s_w} \right) a_{max}^* + \left[\frac{(L_0s)^2}{2s_w} - \frac{(L_0s)^2}{2s} - S_{ISW} \right] = 0. \quad (4.4)$$

The a_{max}^* value can be obtained by solving (4.4). The waveform is curved at the maximum interface displacement (figure 9a), and approximating the shape as a triangle will skew the calculated results. Therefore, the inscribed circle of the triangle (the triangle enclosed by the left-hand waveform and the chain line in figure 10) is used to approximate the waveform near the maximum interface displacement and then calculate the modified maximum interface descent (a_{max}^{**}). A comparison of the predicted (a_{max}^{**}) and experimentally measured (a_{max}) results is shown in figure 11(a).

For (4.4), the predictions from the implementation of the geometric approximation are applicable only to the case where the rear face of the wave is overturned. Therefore, to broaden the parameter range, another prediction method based on (1.3) is introduced by considering that the increase in the wave amplitude is influenced by the wavelength and the topographic scale. Considering the impact of the topographic slope, (1.3) is assumed to be accurate as s tends to 0. As s tends to infinity, it is similar to a wave impinging on a vertical wall (undergoes total reflection), and the maximum interface descent is assumed to be twice the incident amplitude, written as $a_{ef0} = \sqrt{2saL_w}/(1 + \sqrt{s/2s_w})$ ($s \rightarrow 0$, $a_{ef0} =$

$\sqrt{2saL_w}$; $s \rightarrow \infty$, $a_{ef0} = 2a$). At the same time, considering the effect of the topographic height on the wave–ridge interaction, the degree of blocking was included to correct the result, written as $2B$, $B = H_r/h_2$. The newly established empirical formula is

$$a_{ef} = \frac{\sqrt{2saL_w}}{1 + \sqrt{\frac{s}{2s_w}}} 2B. \quad (4.5)$$

The comparison between the predicted (a_{ef}) and experimental results is shown in [figure 11\(b\)](#). This empirical formula applies to all the results of this experiment, regardless of whether the ISWs break over the ridge.

4.2. New breaking criterion

The blockage parameter is calculated from the incident wave, but the interface descent increases significantly or slightly for different wave shoaling conditions ([figures 2 and 5](#)). Therefore, to better evaluate the wave–ridge interaction, the maximum interface descent, which can be determined from the initial parameters, is introduced to modify the blockage parameter (ζ_m , modified blockage parameter, replacement of incident amplitude by maximum interface descent) to obtain the effective blockage parameter before ISW breaking:

$$\zeta_m = \frac{a_{max} + h_1}{h_1 + h_2 - H_r}. \quad (4.6)$$

As shown in [figure 12](#), ζ_m provides a clear separation of the types of wave–ridge interactions. Although the maximum interface descent increases slightly for plunging breaking, the maximum interface descent for the transition state is almost unchanged. Therefore, for plunging breaking, ζ_m will be greater than ζ , and for the transition state, ζ_m is essentially consistent with ζ . For this reason, $\zeta_m = 0.65$ can be used to distinguish plunging breaking and the transition state ([figure 12](#)). Here, $\zeta_m = 1$ implies that the maximum interface descent is just enough to touch the top of the ridge; hence plunging–collapsing breaking occurs for $\zeta_m > 1$. In addition, $\zeta_m = 0.50$ can also distinguish the no breaking and transition states. As a result, the modified blockage parameter has a clear physical meaning. Nevertheless, the type of wave–ridge interaction is almost independent of Ir . The relationship between the type of interaction and ζ_m suggests that the degree of interaction is largely dependent on the distance between the wave trough and the ridge crest. And Ir only acts as an adjustment to the blockage parameter (note that Ir is related to the topographic slope, which can modify a_{max}).

Notably, plunging–collapsing breaking ($\zeta_m \approx 0.8$) occurs in the interval of the distribution of plunging breaking ($0.65 < \zeta_m < 1.00$) when $Ir > 1.3$. The two triangles in [figure 12](#) (for $\zeta_m \approx 0.8$, $Ir = 1.40$ and $Ir = 2.20$) correspond to the case of minimum amplitudes at $h_2 = 0.20$ m, with $s = 0.33$ and $s = 0.50$, respectively. At this depth, $h_2 - H_r = 4$ cm, the narrow lower layer channel as the ISW passes through leads to significant enhancement of the lower flow velocity, which can cause plunging–collapsing breaking even when ζ_m does not reach 1 (the lower layer is only 1.6 cm wide at $\zeta_m = 0.8$ for this stratification condition). In the case of the circle at $\zeta_m = 0.70$ and $Ir = 1.63$, a stronger vortex is generated at the top of the wave tail. However, no overall overturning occurs at the rear face of the wave, so we still define it as a transition state. For this and a few other cases, the interaction types will deviate slightly from the criterion.

In this experiment, the interaction of the mode-1 ISW with the ridge is similar to the shoaling and breaking of the mode-2 ISW, particularly the vortex structure at the top

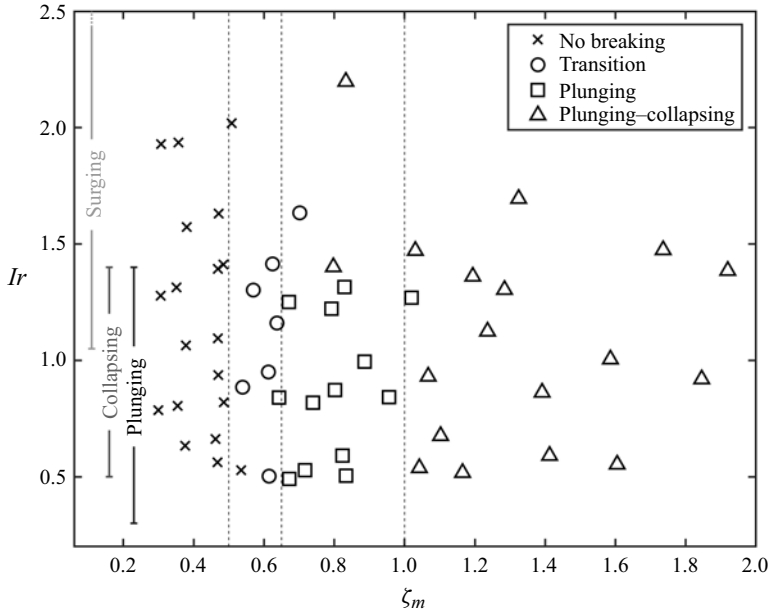


Figure 12. Types of wave–ridge interactions in relation to ζ_m and Ir . The three vertical dashed lines correspond to $\zeta_m = 0.50$, $\zeta_m = 0.65$ and $\zeta_m = 1.00$. Crosses indicate no breaking, hollow circles indicate the transition state, squares indicate plunging breaking, and triangles indicate plunging–collapsing breaking. The segments of lines on the left show the distribution intervals of the type of breaking of the ISW on a uniform slope and the corresponding Ir . With reference to Aghsaee *et al.* (2010) and Sutherland *et al.* (2013), the slope range is $s = 0.15\text{--}0.42$.

of the ridge and the bottom boundary (Deepwell *et al.* 2017, 2019; Carr *et al.* 2019). Deepwell *et al.* (2017) demonstrated that the interaction between mode-2 ISWs and narrow ridges occurs rapidly, with an initial evolution of the lower half similar to that of mode-1 wave–ridge interactions, and that the dimensionless parameters for assessing the interaction strength are essentially the same. Hence the newly established modified blockage parameter can also be extended. Nevertheless, there are discrepancies in the evolution of the two modes: as the lower half-waveform varies, the upper half-layer becomes unstable, thus the subsequent development of mode-2 ISWs will involve different processes, such as the shear instability confined in the pycnocline (Deepwell *et al.* 2019, their figure 13).

4.3. Energy distribution

As the ISW passes over the ridge, a portion of the energy dissipates over the topography, increasing local turbulent mixing, and the remaining energy propagates away from the ridge in the form of reflected and transmitted waves. The energy dissipation, transmission and reflection coefficients of the wave–ridge interaction can be calculated by the equations

$$E_{loss} = E_i - E_r - E_t, \tag{4.7}$$

$$T = \frac{E_t}{E_i}, \tag{4.8}$$

$$R = \frac{E_r}{E_i}, \tag{4.9}$$

where E_i is the incident wave energy, E_r is the reflected energy, and E_t is the transmitted energy. As large-region flow field measurements were carried out in this experiment, the kinetic energy is used to calculate the incident, reflected and transmitted wave energy (2.4). For steadily propagating nonlinear ISWs of moderate amplitude, the kinetic energy is slightly greater than the available potential energy (Lamb & Nguyen 2009; Sutherland *et al.* 2015). Based on the numerical results of Lamb & Nguyen (2009), the kinetic energy in the parameter range of this experiment is slightly greater than 5%–15% of the available potential energy; therefore (2.4) is used to calculate the transmission and reflection coefficient.

The numerical results of Sutherland *et al.* (2015) and the supplementary material (figures S8–S10) show that the reflection coefficient is significantly dependent on the topographic slope, with coefficient differences of up to 0.4 ($s = 0.02$ – 0.16) at different slopes for the same dimensionless amplitude, indicating that different fitting relationships exist between different slopes.

The new breaking criterion proposed in § 4.2 can effectively characterize the degree of wave–ridge interaction. Therefore, the modified blockage parameter is introduced to diagnose the energy distribution. The blockage parameter can be understood as a dimensionless amplitude since (4.6) contains one power term for the amplitude (maximum interface descent). Therefore, the modified blocking parameter is squared to describe the reflected and transmitted energy.

As shown in figure 13(b), the reflection coefficient is no longer dependent on the topographic slope and satisfies a tight linear relationship with ζ_m^2 . The linear fitting result is $R = 0.097\zeta_m^2 - 0.061$. With the introduction of the modified blockage parameter, the dependence of the reflection coefficient on the topographic slope is implicit in the a_{max} that can be calculated from the initial parameters, which can improve the parametrized relationship. The transmission coefficient decreases monotonically with increasing ζ_m^2 , which is also independent of the topographic slope, and satisfies the linear relationship at $\zeta_m^2 < 1.5$ (figure 13a). Both the modified blockage parameter and the predicted maximum interface displacement can be obtained from the initial conditions so that the energy reflection and transmission coefficients can be calculated directly before the wave–ridge interaction.

5. Summary and conclusion

This paper calculates and analyses the shoaling and breaking process of ISW interactions with Gaussian ridges by means of systematic experiments. The type of breaking, breaking time scales, horizontal location of breaking, maximum interface vertical displacement, and energy distribution are evaluated. In the case of gentler topography, the ISW varies slowly during shoaling. Weakly nonlinear theory is capable of describing the evolution process (Zhao *et al.* 2003; Talipova *et al.* 2015; Bai *et al.* 2019). Consequently, this study focuses on the analysis of strong wave–topography interactions where the topographic scale is comparable to the ISW wavelength. Although the spatial distribution of steeper topography in the ocean is relatively limited, energy evolution processes are significant and play an important role in ocean mixing and the energy budget. For example, when ISWs pass over bumpy topography and underwater banks, the energy decays rapidly and generates high-frequency waves (Vlasenko 2005; Xie *et al.* 2019). During ISW interactions with the fjord, noticeable reflected waves can be observed (Bourgault *et al.* 2011) ($s \approx 0.55$). The shoaling and breaking of ISWs on shelf breaks, such as the shallow shelf slope of Dongsha, can result in significant mixing (Davis *et al.* 2020; Sinnett *et al.* 2022) ($s \approx 0.15$).

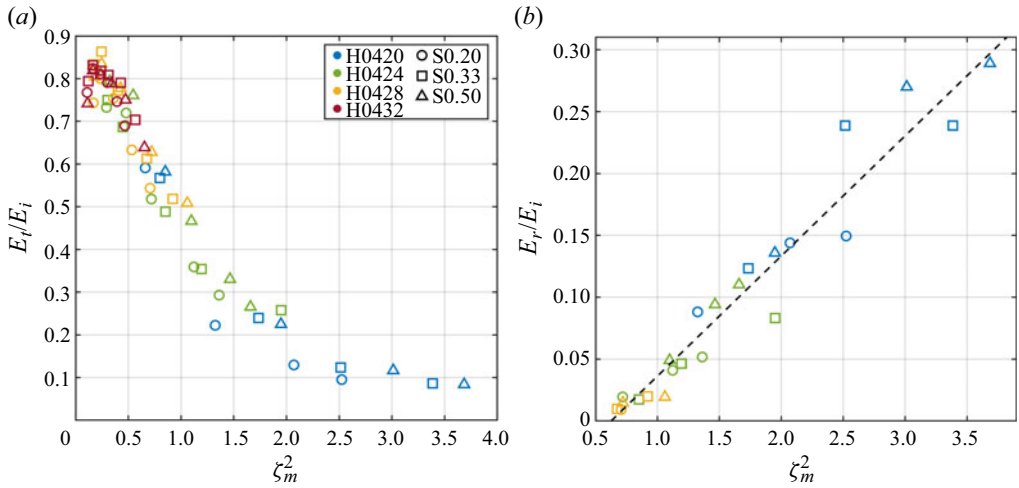


Figure 13. (a) Modified blockage parameter versus transmission coefficient. (b) Modified blockage parameter versus reflection coefficient. The legend is the same as in figure 11. The dashed line in (b) is the linear fit of the experimental results, where $R = 0.097\zeta_m^2 - 0.061$ and $r^2 = 0.94$.

In the parameter space of this experiment, five types of interactions have been observed: weak interaction, fission, transition, plunging breaking and plunging–collapsing breaking. Regarding the type of breaking of ISWs on ridges, the maximum Fr during the wave–ridge interaction provides a clear distinction between the different interaction types. Similarly, the dimensionless parameter ζ , which characterizes the strength of the internal waves with the ridge, is used to distinguish between different shoaling and breaking processes. Convective instability and shear instability are typical dynamical processes during the shoaling of internal waves. In this experiment, convective instability occurs in plunging breaking and plunging–collapsing breaking. However, Kelvin–Helmholtz-like billows were observed not only in high-resolution experiments but also under conditions where the ridge slope was 0.20 and the incident amplitude was large, possibly because the gentler slopes allowed sufficient time for wave shoaling to generate instability.

The maximum interface descent before ISW breaking is predicted in this paper using two methods. The analysis of types of interaction and energy distribution reveals that the degree of the ISW interacting with the ridge can be described in terms of the blockage parameter modified by the maximum interface descent. With the introduced modified blockage parameter, the dependence of the reflection coefficient on the topographic slope is implicit in the a_{max} that can be calculated from the initial parameters. The reflection coefficient satisfies a tight linear relationship with ζ_m^2 , and the transmission coefficient decreases monotonically with increasing ζ_m^2 , which is also independent of the topographic slope, allowing the parametrization scheme of the energy distribution to be optimized.

Within this experiment, the topographic scale is comparable to the ISW scale, resulting in a relatively noticeable change in the maximum interfacial descent of the ISW, which adjusts ζ_m . However, when the topographic scale is considerably larger than the ISW scale (gentle slopes), the ISW has sufficient time to adjust the waveform and undergo fission or polarity transformation. This implies that the maximum interface descent prediction scheme proposed in this experiment needs to be revisited. In the case where the maximum interfacial descent is known (measured directly or predicted by other methods), ζ_m can still be used as a criterion for the type of wave–ridge interaction. However, the applicability of ζ_m in energy distribution needs to be re-evaluated.

The quasi two-layer assumption in this experiment is commonly used in laboratory experiments and numerical simulations. Although this assumption has also been applied in many *in situ* observations, the evolutionary process of ISWs is affected under certain stratifications. For instance, the surface stratification and the broad tanh profile can inhibit the breaking of ISWs (Hartharn-Evans *et al.* 2021), and the near-bottom stratification provides a means for an enhanced rate of three-dimensionalization of jet roll-up instability (Harnanan *et al.* 2017). Therefore, the applicability of the quasi two-layer system should be considered in observations.

Laboratory scale simulations can satisfy geometrical similarity with the steeper topography in the ocean, allowing parameters such as ζ , Ir and Fr to have a similar distribution space. However, the differences in the wave Reynolds numbers between the laboratory and the ocean and lake environments are approximately 3–4 orders of magnitude (Aghsaei *et al.* 2010; Boegman & Stastna 2019). Even with an increase in water depth and density differences in laboratory experiments, the wave Reynolds number remains significantly smaller than that at the field scale (Aghsaei *et al.* 2010; Aghsaei & Boegman 2015). Consequently, the laboratory is focused primarily on the provision of evolutionary processes such as shoaling, deformation, and initial 2-D vortex generation, which can be analogous to real ocean processes. Nevertheless, there is a noticeable scale disparity between the laboratory and the ocean as the 2-D vortex transforms into a 3-D process of splitting into smaller vortices that ultimately dissipate as heat. Compared to the ocean scale, the gap between the length scale of the ISW and the Kolmogorov scale is unrealistically small in the laboratory (Aghsaei *et al.* 2010). At the field scale, multiscale dynamic processes are involved in ISW breaking (Fritts *et al.* 2016; Dorostkar, Boegman & Pollard 2017; Boegman & Stastna 2019).

Supplementary material. Supplementary material is available at <https://doi.org/10.1017/jfm.2024.692>.





Acknowledgements. We thank X. He and T. Xu for their help in carrying out the experiments and for reviewing and editing the original manuscript. Several anonymous individuals are thanked for contributions to these instructions.

Funding. This work was supported by the National Natural Science Foundation of China through grant 41876015 (X.C.), the National Key Research and Development Program of China through grant 2021YFC3101603 (X.C.) and the National Natural Science Foundation of China through grant 42176244 (Q.L.).

Declaration of interests. The authors report no conflict of interest.

Data availability statement. Experimental data supporting the findings of this study are publicly available at <https://doi.org/10.5281/zenodo.7771557>.

Author ORCIDs.

-  Yulin Guo <https://orcid.org/0009-0007-3472-4065>;
-  Xu Chen <https://orcid.org/0000-0001-8526-9612>;
-  Qun Li <https://orcid.org/0000-0001-8767-4179>;
-  Jing Meng <https://orcid.org/0009-0000-8070-956X>.

Author contributions. Y.G. performed the experiments and analysed the experimental data, wrote the original draft and was responsible for visualization. X.C. supervised the project and was responsible for the experimental methodology, resource provision and funding acquisition. Q.L. was responsible for guiding the data analysis, organizing the content of the manuscript, providing resources and funding acquisition. J.M. was responsible for experimental design and procurement of experimental equipment, and participated in experiments. All authors contributed to study conceptualization and design, and reviewed and edited the manuscript.

Appendix A. Sketch of ISW breaking

A sketch of the four stages of ISW breaking associated with figure 2 is shown in figure 14.

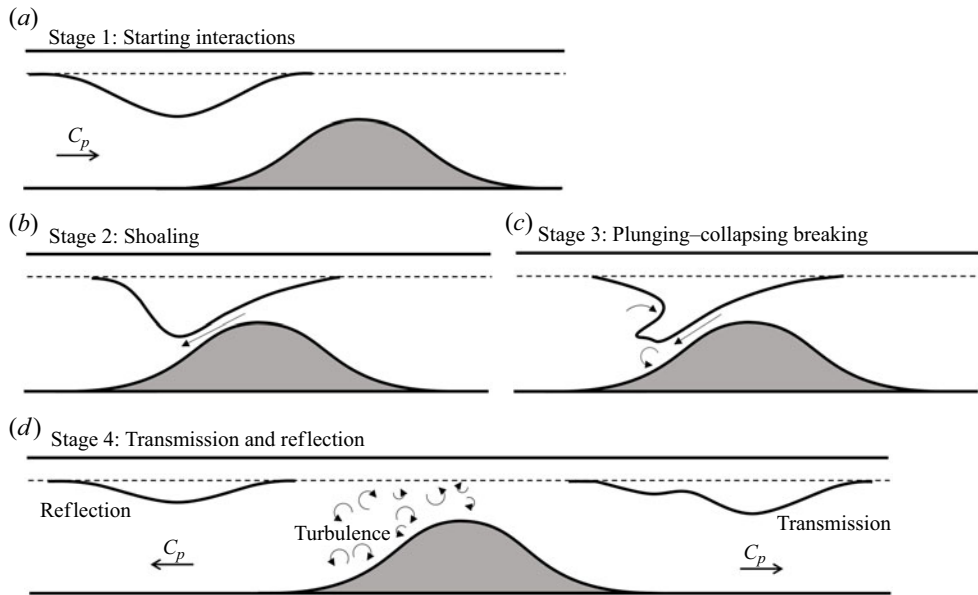


Figure 14. Sketch of the four stages of ISW breaking associated with figure 2.

REFERENCES

- AGHSAEE, P. & BOEGMAN, L. 2015 Experimental investigation of sediment resuspension beneath internal solitary waves of depression. *J. Geophys. Res.: Oceans* **120** (5), 3301–3314.
- AGHSAEE, P., BOEGMAN, L. & LAMB, K.G. 2010 Breaking of shoaling internal solitary waves. *J. Fluid Mech.* **659**, 289–317.
- ALFORD, M.H., LIEN, R.C., SIMMONS, H., KLYMAK, J., RAMP, S., YANG, Y.J., TANG, D. & CHANG, M.H. 2010 Speed and evolution of nonlinear internal waves transiting the South China Sea. *J. Phys. Oceanogr.* **40** (6), 1338–1355.
- ARTHUR, R.S. & FRINGER, O.B. 2014 The dynamics of breaking internal solitary waves on slopes. *J. Fluid Mech.* **761**, 360–398.
- BAI, X., LIU, Z., ZHENG, Q., HU, J., LAMB, K.G. & CAI, S. 2019 Fission of shoaling internal waves on the northeastern shelf of the South China Sea. *J. Geophys. Res.: Oceans* **124** (7), 4529–4545.
- BARAD, M.F. & FRINGER, O.B. 2010 Simulations of shear instabilities in interfacial gravity waves. *J. Fluid Mech.* **644**, 61–95.
- BOEGMAN, L., IVEY, G.N. & IMBERGER, J. 2005 The degeneration of internal waves in lakes with sloping topography. *Limnol. Oceanogr.* **50** (5), 1620–1637.
- BOEGMAN, L. & STASTNA, M. 2019 Sediment resuspension and transport by internal solitary waves. *Annu. Rev. Fluid Mech.* **51** (1), 129–154.
- BOGUCKI, D. & GARRETT, C. 1993 A simple model for the shear-induced decay of an internal solitary wave. *J. Phys. Oceanogr.* **23** (8), 1767–1776.
- BOURGAULT, D., JANES, D.C. & GALBRAITH, P.S. 2011 Observations of a large-amplitude internal wave train and its reflection off a steep slope. *J. Phys. Oceanogr.* **41** (3), 586–600.
- BOURGAULT, D. & KELLEY, D.E. 2003 Wave-induced boundary mixing in a partially mixed estuary. *J. Mar. Res.* **61** (5), 553–576.
- BOURGAULT, D. & KELLEY, D.E. 2007 On the reflectance of uniform slopes for normally incident interfacial solitary waves. *J. Phys. Oceanogr.* **37** (5), 1156–1162.
- CACCHIONE, D.A., PRATSON, L.F. & OGSTON, A.S. 2002 The shaping of continental slopes by internal tides. *Science* **296** (5568), 724–727.

Breaking and energy distribution of ISWs over a ridge

- CARR, M., FRANKLIN, J., KING, S.E., DAVIES, P.A., GRUE, J. & DRITSCHEL, D.G. 2017 The characteristics of billows generated by internal solitary waves. *J. Fluid Mech.* **812**, 541–577.
- CARR, M., KING, S.E. & DRITSCHEL, D.G. 2011 Numerical simulation of shear-induced instabilities in internal solitary waves. *J. Fluid Mech.* **683**, 263–288.
- CARR, M., STASTNA, M., DAVIES, P.A. & VAN DE WAL, K.J. 2019 Shoaling mode-2 internal solitary-like waves. *J. Fluid Mech.* **879**, 604–632.
- CAVALIERE, D., LA FORGIA, G., ADDUCE, C., ALPERS, W., MARTORELLI, E. & FALCINI, F. 2021 Breaking location of internal solitary waves over a sloping seabed. *J. Geophys. Res.: Oceans* **126** (2), e2020JC016669.
- CHANG, M.-H., *et al.* 2021 Direct measurements reveal instabilities and turbulence within large amplitude internal solitary waves beneath the ocean. *Commun. Earth Environ.* **2** (1), 15.
- CHEN, C.-Y. 2007 An experimental study of stratified mixing caused by internal solitary waves in a two-layered fluid system over variable seabed topography. *Ocean Engineering* **34** (14–15), 1995–2008.
- CHEN, C.-Y. 2009 Amplitude decay and energy dissipation due to the interaction of internal solitary waves with a triangular obstacle in a two-layer fluid system: the blockage parameter. *J. Mar. Sci. Technol.* **14** (4), 499–512.
- CHEN, C.-Y. 2010 Using discriminant analysis to determine the breaking criterion for an ISW propagating over a ridge. *Environ. Fluid Mech.* **10** (5), 577–586.
- COWEN, E.A. & MONISMITH, S.G. 1997 A hybrid digital particle tracking velocimetry technique. *Exp. Fluids* **22** (3), 199–211.
- DALZIEL, S.B., CARR, M., SVEEN, J.K. & DAVIES, P.A. 2007 Simultaneous synthetic schlieren and PIV measurements for internal solitary waves. *Meas. Sci. Technol.* **18** (3), 533–547.
- DAVIS, K.A., ARTHUR, R.S., REID, E.C., ROGERS, J.S., FRINGER, O.B., DECARLO, T.M. & COHEN, A.L. 2020 Fate of internal waves on a shallow shelf. *J. Geophys. Res.: Oceans* **125** (5), e2019JC015377.
- DEEPWELL, D., STASTNA, M., CARR, M. & DAVIES, P.A. 2017 Interaction of a mode-2 internal solitary wave with narrow isolated topography. *Phys. Fluids* **29** (7), 076601.
- DEEPWELL, D., STASTNA, M., CARR, M. & DAVIES, P.A. 2019 Wave generation through the interaction of a mode-2 internal solitary wave and a broad, isolated ridge. *Phys. Rev. Fluids* **4** (9), 094802.
- DORON, P., BERTUCCIOLI, L., KATZ, J. & OSBORN, T.R. 2001 Turbulence characteristics and dissipation estimates in the coastal ocean bottom boundary layer from PIV data. *J. Phys. Oceanogr.* **31** (8), 2108–2134.
- DOROSTKAR, A., BOEGMAN, L. & POLLARD, A. 2017 Three-dimensional simulation of high-frequency nonlinear internal wave dynamics in Cayuga Lake. *J. Geophys. Res.: Oceans* **122** (3), 2183–2204.
- FARMER, D., ALFORD, M., LIEN, R.-C., YANG, Y.J., CHANG, M.-H. & LI, Q. 2011 From Luzon Strait to Dongsha Plateau: stages in the life of an internal wave. *Oceanography* **24** (4), 64–77.
- FRITTS, D.C., WANG, L., GELLER, M.A., LAWRENCE, D.A., WERNE, J. & BALSLEY, B.B. 2016 Numerical modeling of multiscale dynamics at a high Reynolds number: instabilities, turbulence, and an assessment of Ozmidov and Thorpe scales. *J. Atmos. Sci.* **73** (2), 555–578.
- FRUCTUS, D., CARR, M., GRUE, J., JENSEN, A. & DAVIES, P.A. 2009 Shear-induced breaking of large internal solitary waves. *J. Fluid Mech.* **620**, 1–29.
- GHASSEMI, A., ZAHEDI, S. & BOEGMAN, L. 2021 Bolus formation from fission of nonlinear internal waves over a mild slope. *J. Fluid Mech.* **932**, A50.
- GRIMSHAW, R., PELINOVSKY, E., TALIPOVA, T. & KURKINA, O. 2010 Internal solitary waves: propagation, deformation and disintegration. *Nonlinear Process. Geophys.* **17** (6), 633–649.
- GRIMSHAW, R.H.J., OSTROVSKY, L.A., SHRIRA, V.I. & STEPANYANTS, Y.A. 1998 Long nonlinear surface and internal gravity waves in a rotating ocean. *Surv. Geophys.* **19** (4), 289–338.
- HARNANAN, S., SOONTIENS, N. & STASTNA, M. 2015 Internal wave boundary layer interaction: a novel instability over broad topography. *Phys. Fluids* **27** (1), 016605.
- HARNANAN, S., STASTNA, M. & SOONTIENS, N. 2017 The effects of near-bottom stratification on internal wave induced instabilities in the boundary layer. *Phys. Fluids* **29** (1), 016602.
- HARTHARN-EVANS, S.G., CARR, M., STASTNA, M. & DAVIES, P.A. 2021 Stratification effects on shoaling internal solitary waves. *J. Fluid Mech.* **933**, A19.
- HELFRICH, K.R. 1992 Internal solitary wave breaking and run-up on a uniform slope. *J. Fluid Mech.* **243**, 133–154.
- HELFRICH, K.R. & MELVILLE, W.K. 2006 Long nonlinear internal waves. *Annu. Rev. Fluid Mech.* **38** (1), 395–425.
- HOGG, A.M.C. & IVEY, G.N. 2003 The Kelvin–Helmholtz to Holmboe instability transition in stratified exchange flows. *J. Fluid Mech.* **477**, 339–362.
- HSIEH, C.-M., HWANG, R.R., HSU, J.R.C. & CHENG, M.-H. 2015 Numerical modeling of flow evolution for an internal solitary wave propagating over a submerged ridge. *Wave Motion* **55**, 48–72.
- HUANG, X., CHEN, Z., ZHAO, W., ZHANG, Z., ZHOU, C., YANG, Q. & TIAN, J. 2016 An extreme internal solitary wave event observed in the northern South China Sea. *Sci. Rep.* **6**, 30041.

- HULT, E.L., TROY, C.D. & KOSEFF, J.R. 2011 The mixing efficiency of interfacial waves breaking at a ridge: 1. Overall mixing efficiency. *J. Geophys. Res.* **116** (C2), 2010JC006485.
- JACKSON, C. 2007 Internal wave detection using the moderate resolution imaging spectroradiometer (MODIS). *J. Geophys. Res.* **112** (C11), C11012.
- JONES, N.L., IVEY, G.N., RAYSON, M.D. & KELLY, S.M. 2020 Mixing driven by breaking nonlinear internal waves. *Geophys. Res. Lett.* **47** (19), e2020GL089591.
- KAO, T.W., PAN, F.-S. & RENOUARD, D. 1985 Internal solitons on the pycnocline: generation, propagation, and shoaling and breaking over a slope. *J. Fluid Mech.* **159**, 19–53.
- KUNZE, E. & SANFORD, T.B. 1996 Abyssal mixing: where it is not. *J. Phys. Oceanogr.* **26** (10), 2286–2296.
- LA FORGIA, G., ADDUCE, C. & FALCINI, F. 2018 Laboratory investigation on internal solitary waves interacting with a uniform slope. *Adv. Water Resour.* **120**, 4–18.
- LAMB, K.G. 2002 A numerical investigation of solitary internal waves with trapped cores formed via shoaling. *J. Fluid Mech.* **451**, 109–144.
- LAMB, K.G. 2003 Shoaling solitary internal waves: on a criterion for the formation of waves with trapped cores. *J. Fluid Mech.* **478**, 81–100.
- LAMB, K.G. 2014 Internal wave breaking and dissipation mechanisms on the continental slope/shelf. *Annu. Rev. Fluid Mech.* **46** (1), 231–254.
- LAMB, K.G. & FARMER, D. 2011 Instabilities in an internal solitary-like wave on the Oregon Shelf. *J. Phys. Oceanogr.* **41** (1), 67–87.
- LAMB, K.G. & NGUYEN, V.T. 2009 Calculating energy flux in internal solitary waves with an application to reflectance. *J. Phys. Oceanogr.* **39** (3), 559–580.
- LIAO, Q., BOOTSMA, H.A., XIAO, J., KLUMP, J.V., HUME, A., LONG, M.H. & BERG, P. 2009 Development of an *in situ* underwater particle image velocimetry (UWPIV) system. *Limnol. Oceanogr.: Methods* **7** (2), 169–184.
- LIEN, R.-C., HENYAY, F., MA, B. & YANG, Y.J. 2014 Large-amplitude internal solitary waves observed in the northern South China Sea: properties and energetics. *J. Phys. Oceanogr.* **44** (4), 1095–1115.
- LIN, Y.-T., LUO, Y., YU, J., SONG, J. & YUAN, Y. 2021 Laboratory investigation of turbulent dissipation in an internal solitary wave breaking over a submerged Gaussian ridge. *Phys. Fluids* **33** (9), 096602.
- MADERICH, V., TALIPOVA, T., GRIMSHAW, R., TERLETSKA, K., BROVCHENKO, I., PELINOVSKY, E. & CHOI, B.H. 2010 Interaction of a large amplitude interfacial solitary wave of depression with a bottom step. *Phys. Fluids* **22** (7), 076602.
- MICHALET, H. & IVEY, G.N. 1999 Experiments on mixing due to internal solitary waves breaking on uniform slopes. *J. Geophys. Res.: Oceans* **104** (C6), 13467–13477.
- MOUM, J.N., FARMER, D.M., SMYTH, W.D., ARMI, L. & VAGLE, S. 2003 Structure and generation of turbulence at interfaces strained by internal solitary waves propagating shoreward over the continental shelf. *J. Phys. Oceanogr.* **33** (10), 2093–2112.
- NAKAYAMA, K., SATO, T., SHIMIZU, K. & BOEGMAN, L. 2019 Classification of internal solitary wave breaking over a slope. *Phys. Rev. Fluids* **4** (1), 014801.
- ORR, M.H. & MIGNERAY, P.C. 2003 Nonlinear internal waves in the South China Sea: observation of the conversion of depression internal waves to elevation internal waves. *J. Geophys. Res. Oceans* **108** (C3), 3064.
- PINKEL, R. 2000 Internal solitary waves in the warm pool of the western equatorial Pacific. *J. Phys. Oceanogr.* **30** (11), 2906–2926.
- RAFFEL, M. 2015 Background-oriented schlieren (BOS) techniques. *Exp. Fluids* **56** (3), 60.
- RAMP, S.R., PARK, J.H., YANG, Y.J., BAHR, F.L. & JEON, C. 2019 Latitudinal structure of solitons in the South China Sea. *J. Phys. Oceanogr.* **49** (7), 1747–1767.
- RAMP, S.R., YANG, Y.-J., JAN, S., CHANG, M.-H., DAVIS, K.A., SINNETT, G., BAHR, F.L., REEDER, D.B., KO, D.S. & PAWLAK, G. 2022 Solitary waves impinging on an isolated tropical reef: arrival patterns and wave transformation under shoaling. *J. Geophys. Res.: Oceans* **127** (3), e2021JC017781.
- REEDER, D.B., MA, B.B. & YANG, Y.J. 2011 Very large subaqueous sand dunes on the upper continental slope in the South China Sea generated by episodic, shoaling deep-water internal solitary waves. *Mar. Geol.* **279** (1–4), 12–18.
- RIVERA-ROSARIO, G., DIAMESSIS, P.J., LIEN, R.-C., LAMB, K.G. & THOMSEN, G.N. 2020 Formation of recirculating cores in convectively breaking internal solitary waves of depression shoaling over gentle slopes in the South China Sea. *J. Phys. Oceanogr.* **50** (5), 1137–1157.
- RIVERA-ROSARIO, G., DIAMESSIS, P.J., LIEN, R.-C., LAMB, K.G. & THOMSEN, G.N. 2022 Three-dimensional perspective on a convective instability and transition to turbulence in an internal solitary wave of depression shoaling over gentle slopes. *Environ. Fluid Mech.* **23**, 1015–1035.

Breaking and energy distribution of ISWs over a ridge

- SANDSTROM, H. & ELLIOTT, J.A. 1984 Internal tide and solitons on the Scotian Shelf: a nutrient pump at work. *J. Geophys. Res.* **89** (C4), 6415–6426.
- SETTLES, G.S. & HARGATHER, M.J. 2017 A review of recent developments in schlieren and shadowgraph techniques. *Meas. Sci. Technol.* **28** (4), 042001.
- SINNETT, G., RAMP, S.R., YANG, Y.J., CHANG, M.-H., JAN, S. & DAVIS, K.A. 2022 Large-amplitude internal wave transformation into shallow water. *J. Phys. Oceanogr.* **52** (10), 2539–2554.
- SMITH, D.K. 1988 Shape analysis of Pacific seamounts. *Earth Planet. Sci. Lett.* **90** (4), 457–466.
- SONG, Z.J., TENG, B., GOU, Y., LU, L., SHI, Z.M., XIAO, Y. & QU, Y. 2011 Comparisons of internal solitary wave and surface wave actions on marine structures and their responses. *Appl. Ocean Res.* **33** (2), 120–129.
- SUTHERLAND, B.R., BARRETT, K.J. & IVEY, G.N. 2013 Shoaling internal solitary waves. *J. Geophys. Res.: Oceans* **118** (9), 4111–4124.
- SUTHERLAND, B.R., KEATING, S. & SHRIVASTAVA, I. 2015 Transmission and reflection of internal solitary waves incident upon a triangular barrier. *J. Fluid Mech.* **775**, 304–327.
- SVEEN, J.K., GUO, Y., DAVIES, P.A. & GRUE, J. 2002 On the breaking of internal solitary waves at a ridge. *J. Fluid Mech.* **469**, 161–188.
- TALIPOVA, T.G., KURKINA, O.E., ROUVINSKAYA, E.A. & PELINOVSKY, E.N. 2015 Propagation of solitary internal waves in two-layer ocean of variable depth. *Izv. Atmos. Ocean. Phys.* **51** (1), 89–97.
- THIELICKE, W. 2014 The flapping flight of birds: analysis and application. PhD thesis, University of Groningen.
- THIELICKE, W. & SONNTAG, R. 2021 Particle image velocimetry for MATLAB: accuracy and enhanced algorithms in PIVlab. *J. Open Res. Softw.* **9** (1), 12.
- THIELICKE, W. & STAMHUIS, E.J. 2014 PIVlab – towards user-friendly, affordable and accurate digital particle image velocimetry in MATLAB. *J. Open Res. Softw.* **2** (1), 30.
- TOOLE, J.M., SCHMITT, R.W., POLZIN, K.L. & KUNZE, E. 1997 Near-boundary mixing above the flanks of a midlatitude seamount. *J. Geophys. Res.: Oceans* **102** (C1), 947–959.
- VLASENKO, V. 2005 Generation of secondary internal waves by the interaction of an internal solitary wave with an underwater bank. *J. Geophys. Res.* **110** (C2), C02019.
- VLASENKO, V. & HUTTER, K. 2002 Numerical experiments on the breaking of solitary internal waves over a slope–shelf topography. *J. Phys. Oceanogr.* **32** (6), 1779–1793.
- WALLACE, B.C. & WILKINSON, D.L. 1988 Run-up of internal waves on a gentle slope in a two-layered system. *J. Fluid Mech.* **191**, 419–442.
- WANG, T., HUANG, X., ZHAO, W., ZHENG, S., YANG, Y. & TIAN, J. 2022 Internal solitary wave activities near the Indonesian submarine wreck site inferred from satellite images. *J. Mar. Sci. Engng* **10** (2), 197.
- WANG, X., ZHOU, J.-F., WANG, Z. & YOU, Y.-X. 2018 A numerical and experimental study of internal solitary wave loads on semi-submersible platforms. *Ocean Engng* **150**, 298–308.
- WESSEL, P. 2001 Global distribution of seamounts inferred from gridded Geosat/ERS-1 altimetry. *J. Geophys. Res.: Solid Earth* **106** (B9), 19431–19441.
- WESSELS, F. & HUTTER, K. 1996 Interaction of internal waves with a topographic sill in a two-layered fluid. *J. Phys. Oceanogr.* **26** (1), 5–20.
- XIE, J., HE, Y. & CAI, S. 2019 Bumpy topographic effects on the transbasin evolution of large-amplitude internal solitary wave in the northern South China Sea. *J. Geophys. Res.: Oceans* **124** (7), 4677–4695.
- XU, C. 2015 Numerical simulations of shoaling internal solitary waves of elevation. PhD thesis, University of Waterloo.
- XU, C. & STASTNA, M. 2020 Instability and cross-boundary-layer transport by shoaling internal waves over realistic slopes. *J. Fluid Mech.* **895**, R6.
- XU, C., STASTNA, M. & DEEPWELL, D. 2019 Spontaneous instability in internal solitary-like waves. *Phys. Rev. Fluids* **4**, 014805.
- YANG, Y.J., FANG, Y.C., TANG, T.Y. & RAMP, S.R. 2010 Convex and concave types of second baroclinic mode internal solitary waves. *Nonlinear Process. Geophys.* **17** (6), 605–614.
- ZAHEDI, S. 2021 Energy dissipation from internal solitary waves shoaling on flat and mildly sloping beds. PhD thesis, Queen's University.
- ZHANG, X., HUANG, X., YANG, Y., ZHAO, W., WANG, H., YUAN, C. & TIAN, J. 2023 Energy cascade from internal solitary waves to turbulence via near- N waves in the northern South China Sea. *J. Phys. Oceanogr.* **53** (6), 1453–1466.
- ZHAO, Z., KLEMAS, V.V., ZHENG, Q. & YAN, X.-H. 2003 Satellite observation of internal solitary waves converting polarity. *Geophys. Res. Lett.* **30** (19), 1988.
- ZHU, H., WANG, L., AVITAL, E.J., TANG, H. & WILLIAMS, J.J.R. 2016 Numerical simulation of interaction between internal solitary waves and submerged ridges. *Appl. Ocean Res.* **58**, 118–134.